Title

Deletion of Fmr1 from Forebrain Excitatory Neurons Triggers Abnormal Cellular, EEG, and Behavioral Phenotypes in the Auditory Cortex of a Mouse Model of Fragile X Syndrome

Journal

Cerebral Cortex, 30(3)

ISSN

1047-3211

Authors

Lovelace, Jonathan W
Rais, Maham
Palacios, Arnold R
et al.

Publication Date

2020-03-14

DOI

10.1093/cercor/bhz141

Peer reviewed

Deletion of *Fmr1* from forebrain excitatory neurons triggers abnormal cellular, EEG and behavioral phenotypes in the auditory cortex of a mouse model of Fragile X Syndrome

Jonathan W. Lovelace[1#], Maham Rais[2#], Arnold R. Palacios[2#], Xinghao S. Shuai[2], Steven Bishay[2], Otilia Popa[2], Patricia S. Pirbhoy[2], Devin K. Binder[2,3], David L. Nelson[4], Iryna M. Ethell[2,3]* and Khaleel A. Razak[1,3]*

[1]Department of Psychology; [2]Division of Biomedical Sciences, School of Medicine and [3]Graduate Neuroscience Program, University of California Riverside, Riverside, CA 92521; [4]Baylor College of Medicine, Houston, TX 77030

[#] These authors contributed equally
*Co-Corresponding Authors:
Khaleel A. Razak, PhD
Department of Psychology
Email: Khaleel@ucr.edu
Phone: 951-827-5060

Iryna M. Ethell, PhD
Division of Biomedical Sciences
Email: iryna.ethell@medsch.ucr.edu
Phone: 951-827-2186

Running Title: Mechanisms of auditory cortex deficits in Fragile X Syndrome

Number of Figures: 10
Number of Tables: 4
Supplemental Figure: 1

We report no conflict of interest.

Abstract

Fragile X Syndrome (FXS) is a leading genetic cause of autism with symptoms that include sensory processing deficits. In both humans with FXS and a mouse model (*Fmr1* KO mouse), electroencephalographic (EEG) recordings show enhanced resting state gamma power and reduced sound-evoked gamma synchrony. We previously showed that elevated levels of matrix metalloproteinase-9 (MMP-9) may contribute to these phenotypes by affecting perineuronal nets (PNNs) around parvalbumin (PV) interneurons in the auditory cortex of *Fmr1* KO mice. However, how different cell types within local cortical circuits contribute to these deficits is not known. Here, we examined whether *Fmr1* deletion in forebrain excitatory neurons affects neural oscillations, MMP-9 activity and PV/PNN expression in the auditory cortex. We found that cortical MMP-9 gelatinase activity, mTOR/Akt phosphorylation and resting EEG gamma power were enhanced in $Cre^{Nex1}/Fmr1^{Flox/y}$ cKO mice, whereas the density of PV/PNN cells was reduced. The $Cre^{Nex1}/Fmr1^{Flox/y}$ cKO mice also show increased locomotor activity, but not the anxiety-like behaviors. These results indicate that FMRP changes in excitatory neurons in the cortex are sufficient to elicit cellular, electrophysiological and behavioral phenotypes in *Fmr1* KO mice. More broadly, these results indicate that local cortical circuit abnormalities contribute to sensory processing deficits in autism spectrum disorders.

Keywords: Autism, Cortical Deficits, Fragile X Syndrome, Perineuronal Nets, Sensory Processing Disorders

Fragile X Syndrome (FXS) is a common monogenic form of autism spectrum disorders (ASD) (Crawford et al. 2001). FXS is usually caused by a CGG repeat expansion in 5'-untranslated region of the *Fragile X mental retardation 1* (*Fmr1) gene* with consequent gene methylation, down-regulation of Fragile X Mental Retardation Protein (FMRP), translational dysregulation, and abnormal protein synthesis (Verkerk et al. 1991; Sutcliffe et al. 1992). Symptoms of FXS include anxiety, intellectual disability, repetitive behaviors, social communication deficits, and abnormal sensory processing (Penagarikano et al. 2007; Braat and Kooy 2015). Abnormal sensory processing in FXS includes debilitating hypersensitivity and reduced habituation to sensory inputs, particularly in the auditory domain (Castrén et al. 2003; Schneider et al. 2013; Ethridge et al. 2016). These symptoms are seen early in development, and may lead to cognitive deficits and delayed language.

Auditory hypersensitivity and cortical processing deficits are observed in humans with FXS and the mouse model of FXS, the *Fmr1* knockout (KO) mice (Chen and Toth 2001; Rojas et al. 2001; Nielsen et al. 2002; Castrén et al. 2003; Rotschafer and Razak 2013; Rotschafer and Razak 2014; Ethridge et al. 2016; Sinclair et al. 2017; Rais et al. 2018). Recent studies of EEG recordings from humans and rodents show remarkably similar changes in cortical neural oscillations, including increased resting EEG gamma band power, which may underlie sensory hypersensitivity in FXS (Ethridge et al. 2016; Wang et al. 2017; Lovelace et al. 2018). FMRP is expressed at multiple levels and cell types of the auditory neuraxis, and auditory brainstem deficits are present in global *Fmr1* KO mice (Strumbos et al. 2010; Beebe et al. 2014; Wang et al. 2014; Rotschafer et al. 2015; Garcia-Pino et al. 2017). While EEG recordings show abnormal responses at the cortical level, their origin and cell type specificity are not known.

Our previous studies suggested a novel mechanism for auditory hypersensitivity in FXS. Impaired development of parvalbumin (PV)-expressing inhibitory interneurons may underlie abnormal auditory cortical processing in *Fmr1* KO mice *via* matrix metalloproteinase-9 (MMP-9)-dependent regulation of perineuronal nets (PNNs) (Wen et al. 2018). FMRP negatively regulates MMP-9 translation in neurons (Dziembowska and Wlodarczyk 2012; Dziembowska et al. 2013; Janusz et al. 2013), and MMP-9 levels are elevated in the brain of *Fmr1* KO mice and FXS postmortem brain tissues (Bilousova et al. 2009; Gkogkas et al. 2014; Sidhu et al. 2014; Wen et al. 2018). MMP-9 is secreted from a number of cell types, including astrocytes and neurons (Szklarczyk et al. 2002). MMP-9 can also mediate changes in synaptic functions by signaling through the PI3K/Akt/mTOR pathway (Sidhu et al. 2014), potentially through BDNF/trkB signaling by cleaving pro-BDNF (Hwang et al. 2005; Yang et al. 2009) or activating integrin receptors (Legate et al. 2009; Chen et al. 2010). PI3K/Akt/mTOR pathway is implicated in FXS symptoms (Klann and Dever 2004; Ronesi and Huber 2008; Sharma et al. 2010; Gross et al. 2011; Hoeffer et al. 2012; Enriquez-Barreto and Morales 2016; Sato 2016), Therefore, MMP-9 may contribute to the changes in cortical hyperexcitability of *Fmr1* KO mice by affecting both inhibitory and excitatory neurons. *In vitro* slice recordings showed increased cortical excitability in mouse somatosensory cortex with deletion of *Fmr1* only from excitatory neurons, suggesting that FMRP expression in excitatory cortical neurons is required for normal cortical activity (Hays et al. 2011).

One method to begin understanding the cell-type and circuit-specific mechanisms underlying the phenotypes in a genetic disorder is to remove the gene from specific cell types and circuits. Therefore, the main goal of this study was to determine the neurobehavioral phenotypes following deletion of *Fmr1* from forebrain excitatory neurons. Our data show that

removal of FMRP from forebrain excitatory neurons is sufficient to elicit FXS-associated symptoms including enhanced MMP-9 activity, mTOR/Akt signaling and resting state neural oscillations, impaired PV/PNN expression and hyperactive behaviors. Together, these data suggest novel mechanisms that lead to sensory hypersensitivity in FXS and potentially other autism spectrum disorders.

Methods

Mice

C57Bl/6 *Fmr1* KO mice and their congenic controls were obtained from Jackson Laboratories. In order to delete FMRP specifically from forebrain excitatory neurons, we crossed male Cre^{Nex1} with female $Fmr1^{flox/flox}$ mice to produce male $Cre^{Nex1}/Fmr1^{flox/y}$ conditional knock out (cKO) mice and their wild type (WT) littermates, $Fmr1^{flox/y}$ mice. $Fmr1^{flox}$ mice were obtained from Dr. David Nelson (Baylor College of Medicine, Houston, Texas) (Mientjes et al. 2006). *Nex1(NeuroD6)*-Cre mice (Goebbels et al. 2006) were generated in Dr. Klaus Nave's lab (Göttingen, Germany) and breeding pairs were obtained from Dr. Joshua Sanes' lab (Harvard University). Separate groups of mice were used for EEG recordings, biochemical analysis, and behavior tests. All genotypes were confirmed by PCR analysis of genomic DNA isolated from mouse tails. Mice were maintained in an AAALAC accredited facility under 12 hour light/dark cycle and fed standard mouse chow. All procedures were done according to NIH and Institutional Animal Care and Use Committee guidelines. All procedures were approved by IACUC. Food and water were provided to the mice *ad libitum*.

Methods overview

Goebbels et al., (2006) reported that most of the Cre activity in the Nex-Cre mice was in neocortex and hippocampus, and marked pyramidal neurons of the cortex without affecting inhibitory or glial cells. These mice are often used for generating forebrain excitatory neuron specific deletion of specific genes (Ballester-Rosado et al. 2010; Kazdoba et al. 2012; Kerrisk et al. 2013). To confirm deletion of FMRP in forebrain excitatory neurons, we examined expression of FMRP in the auditory cortex in P60-70 mice using immunostaining. FMRP is also expressed in auditory thalamus and midbrain of WT mice. To ensure that FMRP is deleted specifically in the forebrain, we quantified expression of FMRP in the medial geniculate body and inferior colliculus, major nuclei of the lemniscal auditory thalamus and midbrain, respectively. We also compared the effects of forebrain excitatory neuron specific *Fmr1* deletion to global *Fmr1* KO mice of the same age on PV/PNN expression in adult auditory cortex. This was necessary because our previous study only examined the developing brain (Wen et al. 2018). This was followed by measurements of the effects of FMRP deletion from forebrain excitatory neurons on gelatinase activity and mTOR/Akt phosphorylation in the adult auditory cortex of both global *Fmr1* KO and $Cre^{Nex1}/Fmr1^{Flox/y}$ cKO mice. We also recorded EEG signals from awake, freely moving mice to determine the effects of FMRP deletion from forebrain excitatory neurons on neural oscillations in the adult auditory cortex to compare with our previous study of these phenotypes in global *Fmr1* KO mice (Lovelace et al. 2018). Finally, we examined anxiety-like behaviors and hyperactivity in $Cre^{Nex1}/Fmr1^{Flox/y}$ cKO mice to compare with our previous study of these phenotypes in global *Fmr1* KO mice (Dansie et al. 2013).

Immunofluorescence

Age-matched adult (P60-70) male *Fmr1* KO and WT, or $Cre^{Nex1}/Fmr1^{Flox/y}$ cKO and $Fmr1^{Flox/y}$ mice were euthanized with isoflurane and sodium pentobarbital and perfused transcardially first with cold phosphate-buffered saline (PBS, 0.1 M) to clear out the blood and then with 4% paraformaldehyde (PFA) in 0.1M PBS for fixation. Brains were removed and post-fixed for 2–4h in 4% PFA. 40-100μm brain slices were obtained using a vibratome (5100mz Campden Instruments). Auditory cortex was identified using hippocampal and brain atlas landmarks (Paxinos and Franklin 2004). For each brain, an average of 5–6 brain slices containing auditory cortex, thalamus or inferior colliculus were collected.

Detection of PV/PNN

Immunostaining in 100μm brain slices containing auditory cortex was performed as previously described with minor modifications (Wen et al. 2018). Briefly, brain slices were post-fixed for an additional 2h in 4% PFA in 0.1 M PBS and then washed 3 times in 0.1M PBS for 10 min. Slices were then quenched with 50mM ammonium chloride for 15 min and washed 3 times with PBS for 10 min. Next, brain tissues were permeabilized with 0.1% Triton X-100 in PBS and nonspecific staining was blocked with a 5% Normal Goat Serum (NGS; Sigma, catalog# G9023-10 mL) and 1% Bovine Serum Albumin (BSA; Fisher Scientific, catalog# 9048468) in 0.1M PBS solution. Brain slices were treated overnight with mouse anti-parvalbumin antibody (1:1000; Sigma, catalog# P3088, RRID:AB_477 329) to label parvalbumin-positive (PV) inhibitory interneurons. Wisteria floribunda agglutinin (WFA; 4μg/mL; Vector Laboratories, cat# FL-1351, RRID:AB_2 336875) in 0.1M PBS containing 1% NGS, 0.5% BSA, and 0.1% Tween-20 solution was used to stain for PNNs containing aggrecan, known as WFA+ PNNs. WFA is a lectin, which binds glycosaminoglycan side chains of chondroitin sulfate proteoglycan

aggrecan that is found in PNNs (Pizzorusso et al. 2002). After incubation, brain slices were washed 3 times in 0.1M PBS containing 0.5% Tween-20 for 10 min and incubated with secondary antibody, donkey anti-mouse Alexa 594 (4µg/mL; Thermo Fisher Scientific, catalog# A-21203, RRID:AB_2 535789) in 0.1M PBS for 1h. Slices were then washed 3 times with 0.1M PBS containing 0.5% Tween-20 for 10 min, mounted with Vectashield containing DAPI (Vector Labs, catalog# H-1200, RRID: AB_2336790) and Cytoseal (ThermoScientific, catalog# 8310–16).

Detection of FMRP Expression

Immunostaining for FMRP was performed using antigen retrieval methods, as previously described (Gabel et al. 2004; Christie et al. 2009; Gross et al. 2011), with the following modifications. 40µm brain slices were mounted onto Superfrost Plus Microscope Charged Slides (Fisher Scientific, catalog #22-034-979); washed 3 times with TBS (0.1M Tris Cl pH7.5, 0.15M NaCl) for 10 min; treated with 0.8% Na Borohydride (Sigma S-9125) to reduce background and autofluorescence; and boiled in 0.01M Na Citrate (Citric acid, sodium salt in water pH 6.0, Sigma C-8532) to achieve antigen retrieval. Permeabilization was performed with 0.5% Triton-X 100 for 20 min, and slices were stained overnight with mouse anti-FMRP (1:100; Developmental Studies Hybridoma Bank, catalog #2F5-1-s, RRID: AB_10805421), and rabbit anti-NeuN (1:1000; Abcam, catalog #ab104225, RRID: AB_10711153) in TBS containing 2% Normal Donkey serum (NDS) and 0.1% Triton-X 100. After incubation with primary antibodies, slices were washed 3 times in TBS for 10 min and incubated with secondary antibodies for 1h. Secondary antibodies used were donkey anti-rabbit Alexa 594 (4µg/mL; Thermo Fisher Scientific, catalog# A-21207, RRID:AB_141637), and donkey anti-mouse Alexa 488 (4µg/mL;

Molecular Probes, catalog# A-21202, RRID:AB_141607). Slices were mounted with Vectashield containing DAPI and cytoseal and imaged.

Image Analysis

Slices were imaged using confocal microscopy (Leica SP5) by collecting a series of 20 high-resolution optical sections (1024 × 1024-pixel format) at 1 um step intervals (z-stack) that were captured for each slice using a 10×, 20×, or a 63× water-immersion objective (1.2 numerical aperture), with 1× or 5× zoom. All images were acquired under identical conditions. Each z-stack was collapsed into a single image by projection, converted to a TIFF file, encoded for blind analysis, and analyzed using ImageJ. ImageJ was used to identify and manually count PV-positive cells, WFA-positive PNN cells, PV/PNN co-localization, NeuN-positive cells and FMRP/NeuN co-localization. Cortical layers were identified as previously reported (Anderson et al. 2009) and used for layer-specific analysis. Three slices were used per animal and cell counts were obtained in layers 1–4 of both the right and left auditory cortex (cell density was measured per layer). The freehand selection tool and measure function was used to specify layers of the auditory cortex and the point tool was used to label PNNs, PV cells, and NeuN cells added to the ROI manager. Particle Analysis Cell Counter plugin in Image J was used to count co-localization. Average cell density was calculated for each animal. Because we were comparing different mouse lines, the global *Fmr1* KO and the $Cre^{Nex1}/Fmr1^{Flox/y}$ cKO mice were evaluated against their specific controls (WT and $Fmr1^{Flox/y}$, respectively), and statistical analysis was performed with unpaired t-test using GraphPad Prism 6 software (RRID: SCR_002798). Data represent mean ± standard error of the mean (SEM).

Dye-Quenched (DQ) Gelatin Assay and Analysis

The DQ-Gelatin plate assay was used to assess gelatinase activity. A FITC-quenched gelatin peptide that fluoresces following cleavage by gelatinases MMP-2 and MMP-9 was used to measure gelatinase proteolytic activity. Adult (P60-70) male WT and *Fmr1* KO mice, or $Fmr1^{Flox/y}$ and $Cre^{Nex1}/Fmr1^{Flox/y}$ cKO litter mates (n = 4-6 mice per group) were euthanized with isoflurane and the auditory cortex was dissected based on coordinates (Paxinos and Franklin 2004) and previous electrophysiological and dye-placement studies (Martin del Campo et al. 2012). Auditory cortex tissues were re-suspended in lysis buffer (50mM Tris-HCl, pH 7.4, 150mM NaCl, 5mM EDTA, 0.05% Triton X-100, and 1mM PMSF) containing protease inhibitor cocktail (Sigma, cat. # P8340) and phosphatase inhibitor cocktail (Sigma, cat. #P0044). Lysates were measured for total protein concentrations using the protocol for the BCA colorimetric protein assay (Pierce, cat#23235).

Lysates were diluted in reaction buffer and mixed with a fluorescence-labeled gelatin substrate (Molecular Probes, E12055). Samples were incubated in the dark for 3h at room temperature. The fluorescence intensity was analyzed using 495nm excitation wavelength and 515nm emission wavelength. The signal was measured every 20min during the 3h incubation period using a fluorescence microplate reader equipped with standard fluorescein filters (SoftMax Pro). For each time point, background fluorescence intensity was corrected by subtracting the values derived from reaction buffer control. A standard curve to assess gelatinase activity was generated using recombinant mouse MMP-9 (rmMMP-9, approximately 1,500 pmol/min/μg, R&D Systems, cat. #909-MM-010). A linear regression of rmMMP-9 activity (standard curve) and relative gelatinase activity based on the average fluorescence intensity of five replicates was used to assess gelatinase proteolytic activity in the brain samples. Statistical

analysis was performed comparing KO samples to their corresponding WT samples with unpaired t-test using GraphPad Prism 6 software (RRID: SCR_002798). Data represent mean ± standard error of the mean (SEM).

Western Blot Analysis

The auditory cortex was removed from each mouse (n=4 mice per group), cooled in PBS, and homogenized in ice-cold lysis buffer (50mM Tris-HCl, pH 7.4, 150mM NaCl, 5mM EDTA, 0.05% Triton X-100, and 1mM PMSF) containing protease inhibitor cocktail (Sigma, cat. # P8340) and phosphatase inhibitor cocktail (Sigma, cat. #P0044). The samples were rotated at 4°C for at least 1h to allow for complete cell lysis and then cleared by centrifugation at 13,200 rpm for 15 min at 4°C. Supernatants were isolated and boiled in reducing sample buffer (Laemmli 2× concentrate, S3401, Sigma), and separated on 8–16% Tris-Glycine SDS-PAGE precast gels (EC6045BOX, Life Technologies). Proteins were transferred onto Protran BA 85 Nitrocellulose membrane (GE Healthcare) and blocked for 1h at room temperature in 5% skim milk (catalog #170-6404, Bio-Rad). Primary antibody incubations were performed overnight at 4°C with antibodies diluted in TBS/0.1% Tween-20/5% BSA. The following primary antibodies were used: rabbit anti-mammalian target of rapamycin (mTOR; 7C10; catalog #2983, RRID:AB_2105622); rabbit anti-phospho-mTOR (Ser2481; catalog #2974, RRID:AB_2231885); rabbit anti-Akt (catalog #9272; RRID:AB_10699016); rabbit anti-phospho-Akt (Ser473; catalog #9271, RRID: AB_329825); mouse anti-Aggrecan at 1:200 (Novus, catalog #NB110-6852, RRID: AB_787911); mouse anti-PV (Millipore, catalog #MAB1572, RRID: AB_2174013) and rabbit anti-βactin at 1:2000 (Abcam, catalog #ab8227,

RRID: AB_2305186). All primary antibodies were from Cell Signaling Technology and used at a dilution of 1:1000, unless stated otherwise.

Blots were washed 3 × 10 min with TBS/0.1% Tween-20 and incubated with the appropriate HRP-conjugated secondary antibodies for 1h at room temperature in a TBS/0.1% Tween-20/5% BSA solution. The secondary antibodies used were HRP-conjugated donkey anti-mouse IgG (Jackson ImmunoResearch, catalog #715-035-150, RRID: AB_2340770) or HRP-conjugated goat anti-rabbit IgG (Jackson ImmunoResearch, catalog #111-035-003, RRID: AB_2313567). After secondary antibody incubations, blots were washed 3 × 10min in TBS/0.1% Tween-20, incubated in ECL 2 Western Blotting Substrate (Thermo Scientific, catalog #80196) and a signal was collected with CL-XPosure film (Thermo Scientific, catalog #34090). For re-probing, membrane blots were washed in stripping buffer (2% SDS, 100mM β-mercaptoethanol, 50mM Tris-HCl, pH 6.8) for 30min at 55°C, then rinsed repeatedly with TBS/0.1% Tween-20, finally blocked with 5% skim milk, and then re-probed. Developed films were then scanned, and band density was analyzed by measuring band and background intensity using Adobe Photoshop CS5.1 software (RRID:SCR_014199). Four samples per group (WT vs. *Fmr1* KO or $Fmr1^{Flox/y}$ vs. $Cre^{Nex1}/Fmr1^{Flox/y}$ cKO) were run per blot, and precision/tolerance (P/T) ratios for *Fmr1* KO and $Cre^{Nex1}/Fmr1^{Flox/y}$ cKO samples were normalized to averaged P/T ratios of WT and $Fmr1^{Flox/y}$ samples, respectively. Statistical analysis was performed with unpaired t-test using GraphPad Prism 6 software. Data represent mean ± standard error of the mean (SEM).

Surgery for *in vivo* EEG recordings

Male $Cre^{Nex1}/Fmr1^{Flox/y}$ cKO (n = 9) and their littermate controls $Fmr1^{Flox/y}$ (n = 9) mice were used for the EEG studies. Mice were anesthetized with isoflurane inhalation (0.2-0.5%)

and an injection of ketamine and xylazine (i.p. 80/10 mg/kg), secured in a bite bar, and placed in a stereotaxic apparatus (model 930; Kopf, CA). Artificial tear gel was applied to the eyes to prevent drying. Toe pinch reflex was used to measure anesthetic state every 10min throughout the surgery, and supplemental doses of ketamine and xylazine were administered as needed. Once the mouse was anesthetized, a midline sagittal incision was made along the scalp to expose the skull. A Foredom dental drill was used to drill 1mm diameter holes in the skull overlying the right auditory cortex (-1.6mm, +4.8mm), left frontal lobe (+3.0mm, -1.6mm), and left occipital (-4.2mm, -5.1mm) (coordinate relative to Bregma: anterior/posterior, medial/lateral). Three channel electrode posts from Plastics One (MS333-2-A-SPC) were attached to 1mm stainless steel screws from Plastics One (8L003905201F) and screws were advanced into drilled holes until secure. Special care was taken not to advance the screws beyond the point of contact with the Dura. Dental cement was applied around the screws, on the base of the post, and exposed skull. Triple antibiotic was applied along the edges of the dental cement followed by an injection of subcutaneous Buprenorphine (0.1mg/kg). Mice were placed on a heating pad to aid recovery from anesthesia. A second Buprenorphine injection was administered between 6 and 10 hours after surgery. Mice were then individually housed, returned to the vivarium and monitored daily until the day of EEG recordings. The separation between the last post-surgical Buprenorphine injection and EEG recordings was between 3 and 5 days.

Electrophysiology

Resting and auditory event related potential (ERP) recordings were obtained using the BioPac system (BIOPAC Systems, Inc.) from awake and freely moving mice as published previously (Lovelace et al. 2018). Mice were allowed to habituate to the recording chamber for

15 minutes prior to being connected to the BioPac system. A three-channel tether was connected to the electrode post (implanted during surgery) under brief isoflurane anesthesia. The mouse was then placed inside a grounded Faraday cage after recovery from isoflurane. This tether was then connected to a commutator located directly above the cage. Mice were then allowed to habituate to being connected to the tether for an additional 15 min before EEG recordings were obtained.

The BioPac MP150 acquisition system was connected to two EEG 100C amplifier units (one for each channel) to which the commutator was attached. The lead to the occipital cortex was used as reference for both frontal and auditory cortex screw electrodes. The acquisition hardware was set to high-pass (>0.5Hz) and low-pass (<100Hz) filters. Normal EEG output data were collected with gain maintained the same (10,000x) between all recordings. Data were sampled at a rate of either 2.5 or 5 kHz using Acqknowledge software and down sampled to 1024Hz post hoc using Analyzer 2.1 (Brain Vision Inc.). Sound delivery was synchronized with EEG recording using a TTL pulse to mark the onset of each sound in a train. Resting EEGs were recorded for 5 minutes (no auditory stimuli were presented), followed by recordings in response to auditory stimulation. After these experiments were completed, mice were returned to the colony and euthanized on a later date.

Acoustic Stimulation

All experiments were conducted in a sound-attenuated chamber lined with anechoic foam (Gretch-Ken Industries, Oregon). Acoustic stimuli were generated using RVPDX software and RZ6 hardware (Tucker-Davis Technologies, FL) and presented through a free-field speaker (MF1 Multi-Field Magnetic Speaker; Tucker-Davis Technologies, FL) located 12 inches directly

above the cage. Sound pressure level (SPL) was modified using programmable attenuators in the RZ6 system. The speaker output was ~70dB SPL at the floor of the recording chamber with fluctuation of +/- 3 dB for frequencies between 5 and 35 kHz as measured with a ¼ inch Bruel & Kjaer microphone.

We used acoustic stimulation paradigms that have been previously established in *Fmr1* KO mice (Lovelace et al. 2018), which is analogous to work in humans with FXS (Ethridge et al. 2017). A chirp-modulated signal (henceforth, 'chirp') to induce synchronized oscillations in EEG recordings was used. The chirp is a 2s broadband noise stimulus with amplitude modulated (100% modulation depth) by a sinusoid whose frequencies increase (Up-chirp) or decrease (Down-chirp) linearly in the 1-100 Hz range (Artieda et al. 2004; Purcell et al. 2004; Pérez-Alcázar et al. 2008). The chirp facilitates a rapid measurement of transient oscillatory response (delta to gamma frequency range) to auditory stimuli of varying frequencies and can be used to compare oscillatory responses in different groups in clinical and pre-clinical settings (e.g., (Purcell et al. 2004). Inter-trial coherence analysis (Tallon-Baudry et al. 1996) can then be used to determine the ability of the neural generator to synchronize oscillations to the frequencies present in the stimulus.

To avoid onset responses contaminating phase locking to the amplitude modulation of the chirp, the stimulus was ramped in sound level from 0-100% over 1s (rise time), which then smoothly transitioned into chirp modulation of the noise. Up and Down chirp trains were presented 300 times each (for a total of 600 trains). Both directions of modulation were tested to ensure any frequency specific effects were not due to the frequency transition history within the stimulus. Up- and Down- chirp trains were presented in an alternating sequence. The interval between each train was randomly varied between 1 and 1.5s.

To study evoked response amplitudes and habituation, trains of 100ms broadband noise were presented at two repetition rates, 0.25Hz (a non-habituating rate) and 4Hz (a strongly habituating rate) (Lovelace et al. 2016). Each train consisted of 10 noise bursts and the inter-train interval used was 8 seconds. Each repetition rate was presented 100 times in an alternating pattern (0.25Hz, 4Hz, 0.25Hz, 4Hz, etc.). The onset of trains and individual noise bursts were tracked with separate TTL pulses that were used to quantify latency of response.

Data Analysis

Data were extracted from Acqknowledge and files saved in a file format (EDF) compatible with BrainVision Analyzer 2.1 software. All data were notch filtered at 60Hz to remove residual line frequency power from recordings. EEG artifacts were removed using a semi-automatic procedure in Analyzer 2.1 for all recordings. Less than 20% of data were rejected due to artifacts from any single mouse. Resting EEG data were divided into 1s segments and Fast Fourier Transforms (FFT) were calculated on each segment using 0.5Hz bins and then average power ($\mu V^2/Hz$) was calculated for each mouse from 1-100Hz. Power was then further binned into standard frequency bands: Delta (1-4Hz), Theta (4-10Hz), Alpha (10-13Hz), Beta (13-30Hz), Low Gamma (30-55Hz), and High Gamma (65-100Hz). Responses to chirp trains were analyzed using Morlet wavelet analysis. Chirp trains were segmented into windows of 500ms before chirp onset to 500ms after the end of the chirp sound (total of 3s because each chirp was 2s in duration). EEG traces were processed with Morlet wavelets from 1-100Hz using complex number output (voltage density, $\mu V/Hz$) for ITPC calculations, and power density ($\mu V^2/Hz$) for non-phase locked single trial power (STP) calculations and baseline corrected non-phase locked single trial power (induced power). Wavelets were run with a Morlet parameter of 10 as this

gave the best frequency/power discrimination. This parameter was chosen since studies in humans found most robust difference around 40Hz, where this parameter is centered (Ethridge et al. 2017). To measure phase synchronization at each frequency across trials Inter Trial Phase Coherence (ITPC) was calculated. The equation used to calculate ITPC is:

$$ITPC(f,t) = \frac{1}{n}\sum_{k=1}^{n}\frac{F_k(f,t)}{|F_k(f,t)|}$$

where f is the frequency, t is the time point, and k is trial number. Thus, $F_k(f,t)$ refers to the complex wavelet coefficient at a given frequency and time for the kth trial. There were no less than 275 trials (out of 300) for any given mouse after segments containing artifacts were rejected.

Statistical analysis and definition of movement states

Statistical group comparisons of chirp responses (ITPC and STP) and broadband noise trains (ITPC and induced power) were quantified by wavelet analysis. Analysis was conducted by binning time into 256 parts and frequency into 100 parts, resulting in a 100x256 matrix. Non-parametric cluster analysis was used to determine contiguous regions in the matrix that were significantly different from a distribution of 2000 randomized Monte Carlo permutations based on previously published methods (Maris and Oostenveld 2007). Briefly, if the cluster sizes of the real genotype assignments (both positive and negative direction, resulting in a two-tailed alpha of $p = 0.025$) were larger than 97.25% of the random group assignments, those clusters were considered significantly different between genotypes. This method avoids statistical assumptions about the data and corrects for multiple comparisons.

Because movement can alter cortical gain (Niell and Stryker 2010; Fu et al. 2015), and *Fmr1* KO mice show hyperactivity, a piezoelectric transducer was placed underneath the

recording cage to detect when the mouse was moving. The term 'resting' is used to indicate EEGs recorded in these mice without any specific auditory stimuli. The term 'still' is used to describe resting EEG when the mouse was stationary. The term 'moving' is used to describe resting EEG when the mouse was moving based on a threshold criterion for the piezoelectric signal that was confirmed by analyzing the video recording (under IR light) that was taken throughout the EEG recording procedure. In all cases where genotype means are reported, SEM was used. The genotype differences in resting power were analyzed on 6 dependent variables using one-way Multivariate analysis of co-variance (MANCOVA) with one covariate (movement), Independent Variables (IV): Genotype (*Fmr1*$^{Flox/y}$ *control*, *Cre*^{Nex1}/*Fmr1*$^{Flox/y}$ cKO mice), dependent variables (DV): 6 frequency bins (delta to high gamma). The proportion of time spent moving during the 5-minute recording session was used as a covariate to isolate effects of genotype and control for the effect movement has on cortical gain. When multiple comparisons for MANCOVA were made, genotype comparisons were corrected using Bonferroni adjustments. The divisor for Bonferroni correction for multiple comparisons (for 6 frequency bands) on MANCOVA was set to 6, $\alpha = 0.05/6 = 0.0083$. Data are often expressed and plotted as ratio of control group values to gauge relative differences in various factors using the same scale.

Behavioral Assessments

Open-field test

Anxiety was tested in P60 mice (6 mice per group) by quantifying their tendency to travel to the center of an open field and time spent in thigmotaxis (Yan et al. 2004; Yan et al. 2005). A 72 × 72-cm open-field arena with 50-cm-high walls was constructed from opaque acrylic sheets

with a clear acrylic sheet for the bottom The open field arena was placed in a brightly lit room, and one mouse at a time was placed in a corner of the open field and allowed to explore for 10 min while being recorded with digital video from above. The floor was cleaned with 2–3% acetic acid, 70% ethanol, and water between tests to eliminate odor trails. The mice were tested between the hours of 9:00 A.M. and 1:00 P.M., and this test was always performed prior to the elevated plus maze. The arena was subdivided into a 4 × 4 grid of squares with the middle of the grid defined as the center. A line 4 cm from each wall was added to measure thigmotaxis. Locomotor activity was scored by the analysis of total line crosses and speed as described previously with some modifications (Brown et al. 1999; Yan *et al.* 2005) using TopScan Lite software (Clever Sys., Inc., Reston, VA 20190, USA). A tendency to travel to the center (total number of entries into large and small center squares) and the time in thigmotaxis were used as an indicator of anxiety using TopScan Lite software (CleverSys Inc). The analysis was performed in 5 min intervals for the total 10 min exploration duration. Assessments of the digital recordings were performed blind to the condition. Statistical analysis was performed with unpaired t-test using GraphPad Prism 6 software. Data represent mean ± standard error of the mean (SEM).

Elevated plus maze

The elevated plus maze consisted of four arms in a plus configuration. Two opposing arms had 15-cm tall walls (closed arms), and two arms were without walls (open arms). The entire maze sat on a stand 1 m above the floor. Each arm measured 30 cm long and 10 cm wide. Mice were allowed to explore the maze for 10 min while being recorded by digital video from above. The maze was wiped with 2–3% acetic acid, 70% ethanol and water between each test to eliminate odor trails. This test was always done following the open-field test. TopScan Lite

445 software was used to measure the percent of time spent in open arms and speed. The time spent
446 in open arm was used to evaluate anxiety-like behavior (Carobrez and Bertoglio 2005). The
447 speed and total arm entries were measured to evaluate overall locomotor activity. The analysis
448 was performed in 5 min intervals for the total 10 min exploration duration. Assessments of the
449 digital recordings were done blind to the condition using TopScan Lite software. Statistical
450 analysis was performed with unpaired t-test using GraphPad Prism 6 software. Data represent
451 mean ± standard error of the mean (SEM).
452
453 **Results**
454 In the current study we examined (1) whether the deficits in PV and PNN expression
455 observed in developing auditory cortex of global *Fmr1* KO mice are also seen in adulthood; (2)
456 the effects of FMRP deletion from forebrain excitatory neurons on gelatinase activity, PV/PNN
457 expression and mTOR/Akt phosphorylation in the adult auditory cortex of $Cre^{Nex1}/Fmr1^{Flox/y}$
458 cKO mice; and (3) whether FMRP deletion from forebrain excitatory neurons affects neural
459 oscillations in the auditory cortex of $Cre^{Nex1}/Fmr1^{Flox/y}$ cKO mice, including resting gamma
460 power and evoked gamma synchronization, and elicit abnormal FXS-associated behaviors, such
461 as hyperactivity and anxiety.
462
463 **Reduced PNNs and PV/PNN co-localization were observed in the auditory cortex of adult**
464 **global *Fmr1* KO mice**
465 We recently showed evidence for abnormal development of PV neurons and PNNs in the
466 developing auditory cortex of global *Fmr1* KO mice (Wen et al. 2018). Here, we examined
467 whether the deficits were also seen in the adult auditory cortex of *Fmr1* KO mice. For this, we

468 characterized the density of PV+ cells and fluorescently tagged WFA was used to assess the
469 density of WFA+ PNN-containing cells in L1-4 of adult WT and *Fmr1* KO auditory cortex (Fig.
470 1A-H). Statistical analysis using unpaired t-test revealed that there was a significant reduction in
471 PV cell density in L4 of *Fmr1* KO auditory cortex compared to WT (n=6, $p = 0.0391$, t-test
472 (Table 2; Fig. 1C). However, no significant changes were observed in PV cell density in L2/3 of
473 *Fmr1* KO auditory cortex compared to WT (n=6, $p = 0.2301$, t-test) (Table 2; Fig. 1F). We
474 observed a significant reduction in WFA+ PNN cell density in *Fmr1* KO auditory cortex
475 compared to WT in both L4 (n=6, $p = 0.0003$, t-test) and L2/3 (n=6, $p = 0.0070$, t-test) (Table 2;
476 Fig. 1D, G). We also analyzed the density of PV/PNN double-labeled cells and found that
477 formation of WFA+ PNNs was impaired around PV cells in adult *Fmr1* KO auditory cortex
478 compared to WT in both L4 (n=6, $p = 0.0048$, t-test) and L2/3 (n=6, $p = 0.0151$, t-test) (Table 2;
479 Fig. 1E, H). Taken together, these data demonstrate that similar to what we observed in the
480 developing *Fmr1* KO mice, formation of WFA+ PNNs and PV/PNN co-localization remains
481 impaired in the adult auditory cortex of global *Fmr1* KO mice. These deficits may underlie the
482 enhanced sound driven response in adult global *Fmr1* KO auditory cortex (Rotschafer and
483 Razak, 2013).

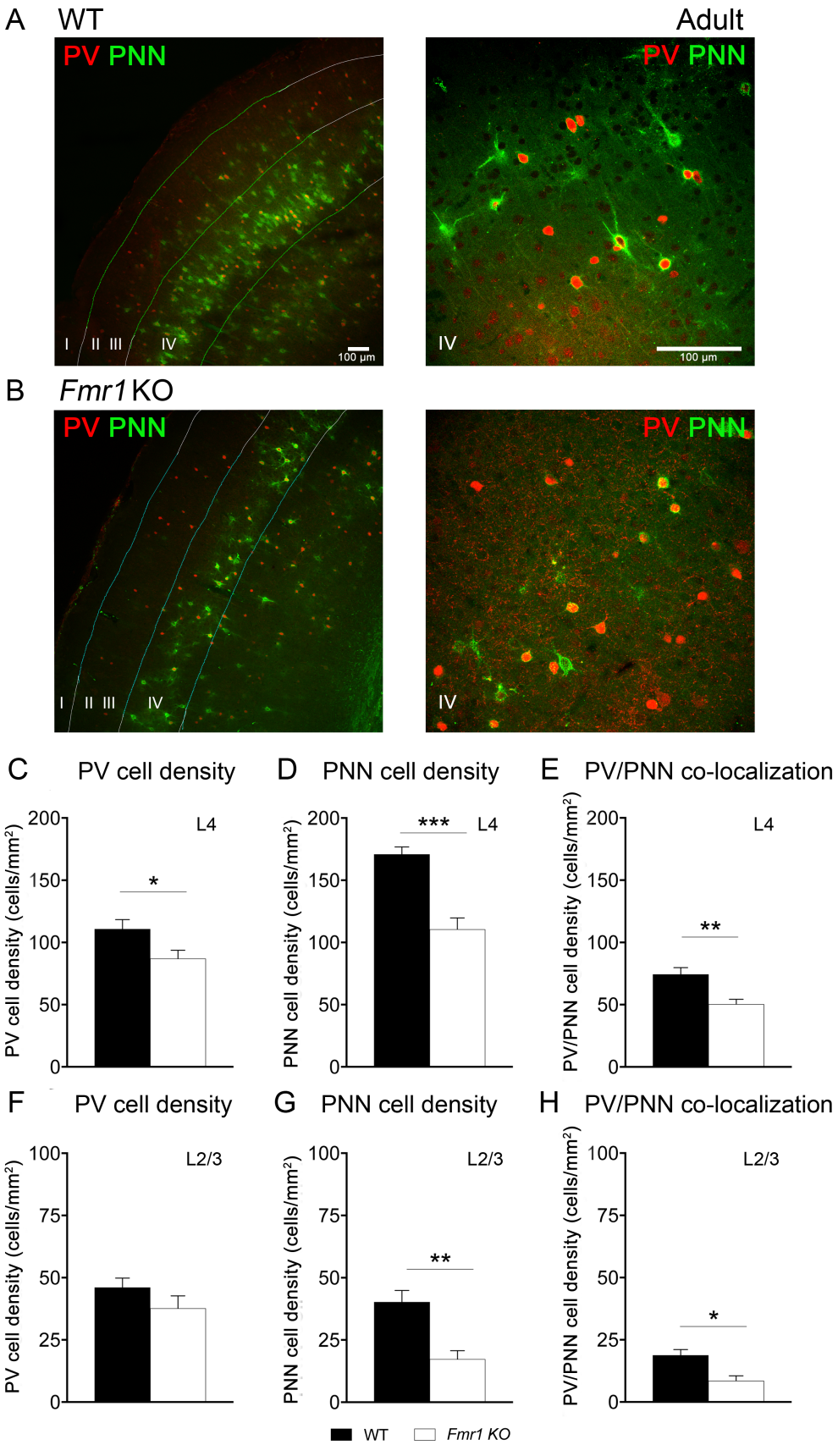
A
WT
Adult
PV PNN
I II III IV
100 µm
IV
B
Fmr1 KO
C
PV cell density
L4
PV cell density (cells/mm²)
D
PNN cell density
PNN cell density (cells/mm²)
E
PV/PNN co-localization
PV/PNN cell density (cells/mm²)
F
L2/3
G
H
WT
Fmr1 KO

Figure 1. Impaired WFA+ PNNs and PV/PNN co-localization are detected in the auditory cortex of adult *Fmr1* KO mice.

(A-B) Confocal images showing PV immunoreactivity (red) and WFA-positive PNN labeling (green) in the auditory cortex of adult WT (A) and *Fmr1* KO mice (B). (C-H) Quantitative analysis of the density of PV, PNN, or PV/PNN positive cells. Graphs show mean ± SEM (n=6/group, *p<0.05; **p<0.01; ***p<0.001, t-test). PV cell density was significantly reduced in L4 auditory cortex of *Fmr1* KO mice compared to WT. (C) No significant changes were observed in PV cell density in L2-3 between the WT and *Fmr1* KO mice (F). PNN cell density was significantly reduced in L4 (D) and L2-3 (G) auditory cortex of *Fmr1* KO mice compared to WT mice (note that only WFA+ cells were counted to measure PNN density). PV/PNN co-localization was also significantly reduced in L4 (E) and L2-3 (H) auditory cortex of *Fmr1* KO mice.

FMRP immunoreactivity was significantly reduced in excitatory neurons of auditory cortex of adult *Cre^{Nex1}/$Fmr1^{Flox/y}$* cKO mice

To achieve the deletion of FMRP from forebrain excitatory neurons, we crossed male Cre^{Nex1} with female *$Fmr1^{flox/flox}$* KO mice and analyzed the expression of FMRP within the regions of the auditory pathway in the *Cre^{Nex1}/$Fmr1^{Flox/y}$* cKO and their littermate controls, *$Fmr1^{Flox/y}$* mice (Fig. 2, Supplementary Fig. 1). *$Fmr1^{Flox/y}$* mice showed FMRP expression in NeuN+ cells (Fig. 2A, D) in the auditory cortex. FMRP immunoreactivity was visibly reduced in the cortex of adult *Cre^{Nex1}/$Fmr1^{Flox/y}$* cKO mice (Fig. 2B, E). No significant changes were observed in NeuN cell density in the *$Fmr1^{Flox/y}$* and *Cre^{Nex1}/$Fmr1^{Flox/y}$* cKO mice (n=3, p=0.6949, t-test) (Table 2; Fig. 2C). However, there was a significant decrease in the percentage of NeuN+

neurons with FMRP in the *Cre*^{Nex1}/*Fmr1*$^{Flox/y}$ cKO mice compared to *Fmr1*$^{Flox/y}$ mice (n=3, p=0.0002, t-test) (Table 1; Fig. 2F). The remaining NeuN+ cells with FMRP are presumed to be GABAergic neurons (Tamamaki et al. 2003). These data confirm that FMRP was deleted from forebrain excitatory neurons in the auditory cortex.

Unlike the auditory cortex, no significant changes in FMRP expression were observed in the inferior colliculus and the auditory thalamus (medial geniculate body; Supplementary Fig. 1). FMRP expression was detected in NeuN+ neurons in the central (Supplementary Fig. 1A-B) and external inferior colliculus (Supplementary Fig. 1D-E), and medial geniculate body (Supplementary Fig. 1G-H) of *Cre*^{Nex1}/*Fmr1*$^{Flox/y}$ cKO mice. No significant changes were observed in the percentage of NeuN+ neurons showing FMRP immunoreactivity in the central (n=3, p=0.0971, t-test; Table 1; Supplementary Fig. 1C) or external inferior colliculus (n=3, p=0.0718, t-test; Table 1; Supplementary Fig. 1F) of *Cre*^{Nex1}/*Fmr1*$^{Flox/y}$ cKO mice compared to *Fmr1*$^{Flox/y}$ mice. In the medial geniculate body as well, no significant changes in the percentage of NeuN+ neurons with FMRP were found between the *Fmr1*$^{Flox/y}$ and *Cre*^{Nex1}/*Fmr1*$^{Flox/y}$ cKO mice (n=3, p=0.6969, t-test; Table 1; Supplementary Fig. 1I). These data confirm a significant loss of FMRP from excitatory neurons in the auditory cortex, but not inferior colliculus or medial geniculate body, of *Cre*^{Nex1}/*Fmr1*$^{Flox/y}$ cKO mice.

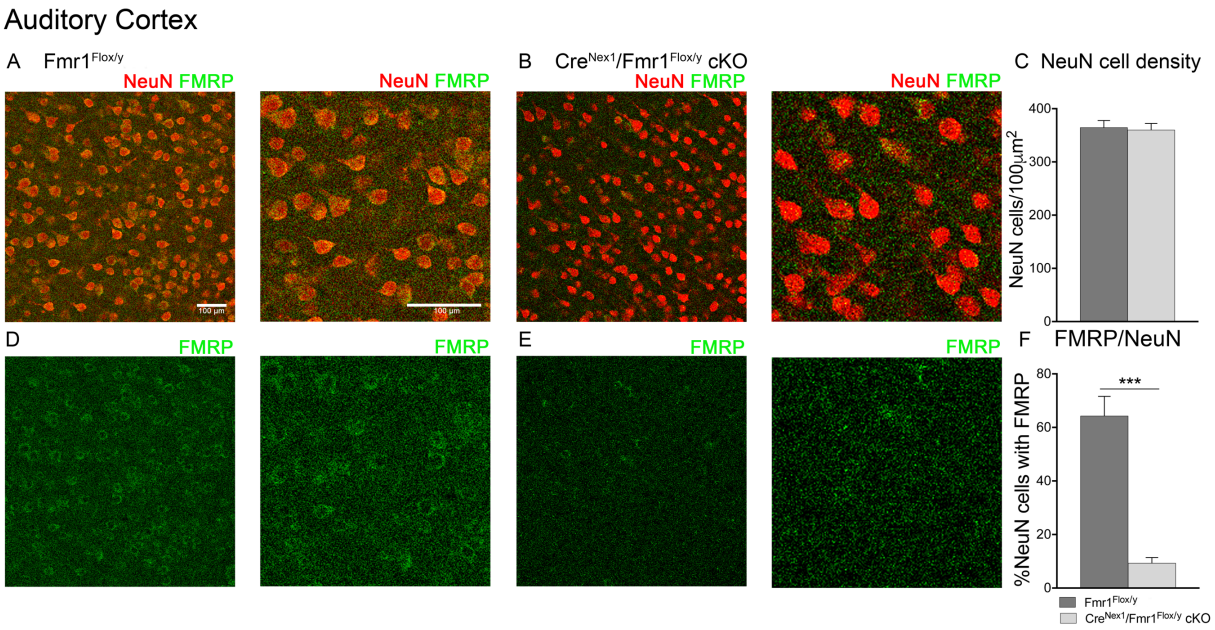

Figure 2. Excitatory specific FMRP loss was observed in the auditory cortex of adult *Cre^{Nex1}/Fmr1$^{Flox/y}$* cKO mice.

(A-B) Confocal images showing NeuN (red) and FMRP (green) immunoreactivity in the auditory cortex of adult *Fmr1*$^{Flox/y}$ and *Cre^{Nex1}/Fmr1$^{Flox/y}$* cKO mice. (C) Quantitative analysis of the density of NeuN-positive cells. Graphs show mean ± SEM. No significant changes were observed in NeuN cell density in the *Fmr1*$^{Flox/y}$ and *Cre^{Nex1}/Fmr1$^{Flox/y}$* cKO mice. (D-E) Confocal images showing FMRP (green) immunoreactivity in the auditory cortex of adult *Fmr1*$^{Flox/y}$ and *Cre^{Nex1}/Fmr1$^{Flox/y}$* cKO mice. (F) Quantitative analysis of the percentage of FMRP-positive NeuN cells. Graphs show mean ± SEM (n= 3/group, ***p<0.001, t-test). There is a significant decrease in the percentage of NeuN+ neurons with FMRP in the *Cre^{Nex1}/Fmr1$^{Flox/y}$* cKO mice compared to *Fmr1*$^{Flox/y}$ mice.

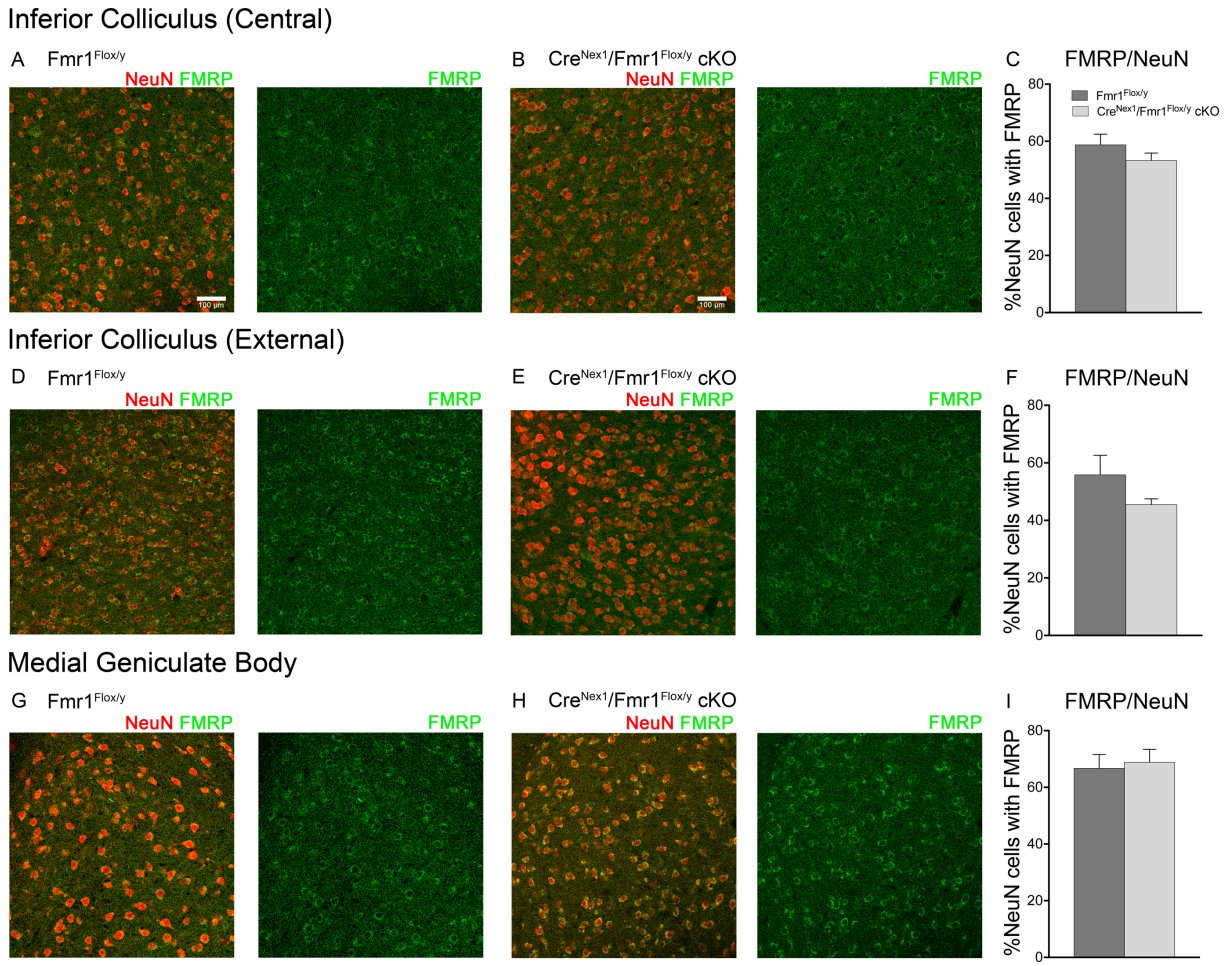

Supplementary Figure 1. FMRP expression remained unchanged in the inferior colliculus and auditory thalamus of adult *Cre^{Nex1}/Fmr1$^{Flox/y}$* cKO mice.

(A-B) Confocal images showing NeuN (red) and FMRP (green) immunoreactivity in the central inferior colliculus of adult *Fmr1*$^{Flox/y}$ and *Cre^{Nex1}/Fmr1$^{Flox/y}$* cKO mice. (C) Quantitative analysis of the density of FMRP-positive cells. Graphs show mean ± SEM (n= 3/group, p>0.05, t-test). No significant changes were observed in the percentage of NeuN+ neurons with FMRP in the *Fmr1*$^{Flox/y}$ and *Cre^{Nex1}/Fmr1$^{Flox/y}$* cKO mice in the central inferior colliculus. (D-E) Confocal images showing NeuN and FMRP immunoreactivity in the external inferior colliculus of adult *Fmr1*$^{Flox/y}$ and *Cre^{Nex1}/Fmr1$^{Flox/y}$* cKO mice. (F) Analysis of the density of FMRP-positive cells. Graphs show mean ± SEM (n= 3/group, p>0.05, t-test). No significant changes were observed in

548 the percentage of NeuN neurons with FMRP in the *Fmr1*$^{Flox/y}$ and *Cre*^{Nex1}/*Fmr1*$^{Flox/y}$ cKO mice in
549 the external inferior colliculus. (G-H) Confocal images showing NeuN and FMRP
550 immunoreactivity in the medial geniculate body of adult *Fmr1*$^{Flox/y}$ and *Cre*^{Nex1}/*Fmr1*$^{Flox/y}$ cKO
551 mice. (I) Analysis of the density of FMRP-positive cells. Graphs show mean ± SEM (n= 3/group,
552 p>0.05, t-test). No significant changes were observed in the percentage of NeuN+ neurons with
553 FMRP in the *Fmr1*$^{Flox/y}$ and *Cre*^{Nex1}/*Fmr1*$^{Flox/y}$ cKO mice in the medial geniculate body of the
554 thalamus.
555
556 **Table 1.** Percentage of NeuN+ neurons with FMRP expression in different regions of the
557 auditory pathway in the *Fmr1*$^{Flox/y}$ and *Cre*^{Nex1}/*Fmr1*$^{Flox/y}$ cKO mice (mean ± SEM).

	Fmr1$^{Flox/y}$	Cre^{Nex1}/*Fmr1*$^{Flox/y}$ cKO
Auditory cortex	64.33 ± 4.188	9.328 ± 1.197
Central inferior colliculus	58.84 ± 2.099	53.3 ± 1.479
External inferior colliculus	53.93 ± 3.88	49.89 ± 2.796
Medial Geniculate Body	66.8 ± 3.40	68.9 ± 3.19

558
559 **Deletion of FMRP from excitatory neurons reduces PV, PNN and PV/PNN co-localization**
560 **in the auditory cortex of adult *Cre*^{Nex1}/*Fmr1*$^{Flox/y}$ cKO mice**
561 We examined PV+ and WFA+ PNN-containing cell density in auditory cortex of adult
562 *Fmr1*$^{Flox/y}$ and *Cre*^{Nex1}/*Fmr1*$^{Flox/y}$ cKO mice (Fig. 3A-H). Similar to the adult *Fmr1* KO mice,
563 there was a significant decrease in PV cell density in auditory cortex of *Cre*^{Nex1}/*Fmr1*$^{Flox/y}$ cKO
564 mice compared to their littermate controls, *Fmr1*$^{Flox/y}$ mice in both L4 (n=6, p = 0.0298, t-test)

and L2/3 (n=6, p = 0.0483, t-test; Table 2; Fig 3C, F). WFA+ PNN cell density was also significantly reduced in auditory cortex of *Cre*^{Nex1}/*Fmr1*$^{Flox/y}$ cKO mice compared to *Fmr1*$^{Flox/y}$ in both L4 (n=6, p <0.0001, t-test) and L2/3 (n=6, p = 0.0002, t-test; Table 2; Fig. 3D, G). In addition, PV/PNN co-localization was significantly decreased in auditory cortex of *Cre*^{Nex1}/*Fmr1*$^{Flox/y}$ cKO mice compared to *Fmr1*$^{Flox/y}$ in L4 (n=6, p = 0.0005, t-test) and L2/3 (n=6, p = 0.0004, t-test; Table 2; Fig. 3E, H). These data indicate that the removal of FMRP from excitatory neurons is sufficient to trigger abnormal development of WFA+ PNNs in the auditory cortex, specifically around inhibitory PV interneurons. Thus, a cell-type specific loss of FMRP may lead to a network-level dysfunction.

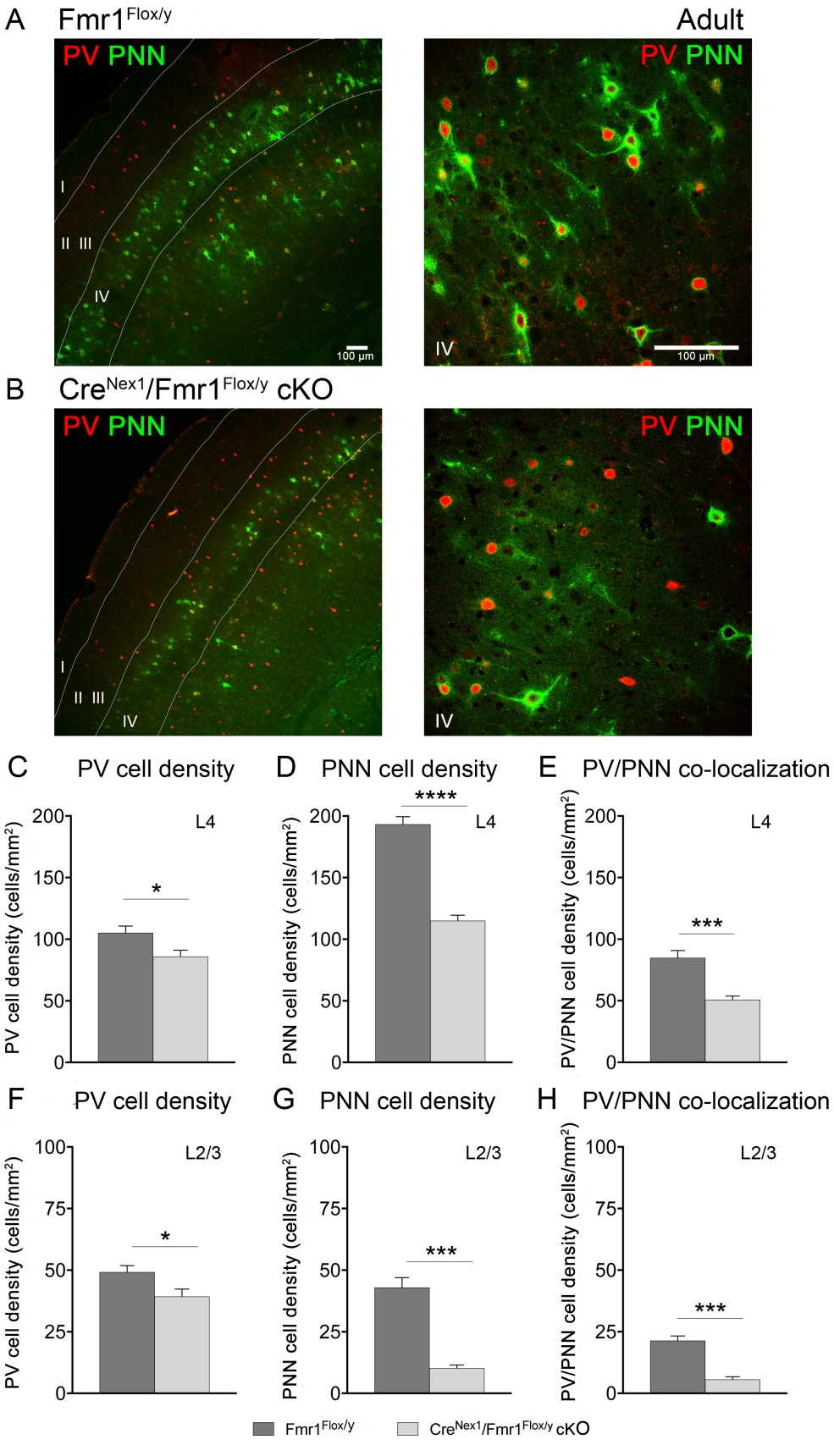
A
Fmr1Flox/y
Adult
PV PNN
I
II III
IV
100 µm
B
CreNex1/Fmr1Flox/y cKO
C
PV cell density
D
PNN cell density
E
PV/PNN co-localization
L4
L2/3
PV cell density (cells/mm2)
PNN cell density (cells/mm2)
PV/PNN cell density (cells/mm2)
*
***
****
F
G
H
Fmr1Flox/y
CreNex1/Fmr1Flox/y cKO

Figure 3. Deletion of *Fmr1* from excitatory neurons affected development of WFA+ PNNs and PV/PNN co-localization in the adult mouse auditory cortex.

(A-B) Confocal images showing PV immunoreactivity (red) and WFA-positive PNN labeling (green) in the auditory cortex of adult *Fmr1*$^{Flox/y}$ (A) and *Cre*^{Nex1}/*Fmr1*$^{Flox/y}$ cKO (B) mice. (C-H) Quantitative analysis of the density of PV, PNN, or PV/PNN positive cells. Graphs show mean ± SEM (n= 6/group, *p<0.05; ***p<0.001; ****p<0.0001, t-test). PV cell density was significantly reduced in L4 (C) and L2-3 (F) auditory cortex of *Cre*^{Nex1}/*Fmr1*$^{Flox/y}$ cKO mice compared to *Fmr1*$^{Flox/y}$. PNN cell density was significantly reduced in L4 (D) and L2-3 (G) auditory cortex of *Cre*^{Nex1}/*Fmr1*$^{Flox/y}$ cKO mice compared to *Fmr1*$^{Flox/y}$ (note that only WFA-positive cells were counted to measure PNN density). PV/PNN co-localization was also significantly reduced in L4 (E) and L2-3 (H) auditory cortex of *Cre*^{Nex1}/*Fmr1*$^{Flox/y}$ cKO mice compared to *Fmr1*$^{Flox/y}$.

Table 2. Density of PV cells, WFA+ PNNs, and PV/PNN co-localization in the auditory cortex of adult WT, *Fmr1* KO, *Fmr1*$^{Flox/y}$, and *Cre*^{Nex1}/*Fmr1*$^{Flox/y}$ cKO mice (mean ± SEM).

	WT		*Fmr1* KO		*Fmr1*$^{Flox/y}$		Cre^{Nex1}/*Fmr1*$^{Flox/y}$ cKO	
	L4	L2/3	L4	L2/3	L4	L2/3	L4	L2/3
PV+ cell density	110.9 ± 7.528	46.06 ± 3.752	87.05 ± 6.65	37.71 ± 5.007	105 ± 5.603	49.2 ± 2.616	85.91 ± 5.064	39.32 ± 3.025
PNN+ cell density	170.8 ± 5.94	40.27 ± 4.639	110.6 ± 9.205	17.35 ± 3.325	193.2 ± 6.189	42.92 ± 4.022	115.1 ± 4.41	10.27 ± 1.221
PV+/PNN+ co-localization	74.31 ± 5.416	18.81 ± 2.282	50.5 ± 3.769	8.562 ± 2.016	84.87 ± 5.924	21.37 ± 1.891	50.8 ± 3.045	5.625 ± 1.104

Total aggrecan levels are reduced, while cleaved aggrecan levels and gelatinase activity are enhanced in the auditory cortex of adult *Cre*^{Nex1}/*Fmr1*$^{Flox/y}$ cKO mice

As enhanced gelatinase activity may contribute to the loss of PNNs by cleaving extracellular matrix (ECM), we performed a gelatinase activity assay. A significant increase in gelatinase activity was observed in both *Fmr1* KO (n=4, $p = 0.0053$, t-test) and $Cre^{Nex1}/Fmr1^{Flox/y}$ cKO mice (n=4, $p = 0.0072$, t-test) as compared to their respective WT counterparts, WT and $Fmr1^{Flox/y}$ mice (Fig. 4A). While the gelatinase activity assay measures both MMP-2 and MMP-9 proteolytic activity, our previous study showed that MMP-2 levels were similar in the adult auditory cortex of WT and *Fmr1* KO mice, while MMP-9 levels were significantly increased in the *Fmr1* KO mice (Lovelace et al., 2016). This suggests that the observed increase in gelatinase activity in adult *Fmr1* KO and $Cre^{Nex1}/Fmr1^{Flox/y}$ cKO mouse auditory cortex could be due to increased MMP-9 levels.

Enhanced gelatinase activity may result in excessive cleavage of aggrecan and a reduction in aggrecan-containing PNNs detected with WFA (Roughley and Mort 2014; Miyata and Kitagawa 2016). Therefore, we next analyzed total and cleaved aggrecan levels in the mouse auditory cortex of adult WT, *Fmr1* KO, $Fmr1^{Flox/y}$ and $Cre^{Nex1}/Fmr1^{Flox/y}$ cKO mice (Fig. 4C). We found that total levels of full-length aggrecan were significantly reduced in both the *Fmr1* KO (n=4, $p = 0.0016$, t-test) and $Cre^{Nex1}/Fmr1^{Flox/y}$ cKO mice (n=4, $p = 0.0159$, t-test) compared to WT and $Fmr1^{Flox/y}$ mice, respectively (Table 3; Fig. 4D). In contrast, cleaved aggrecan levels were significantly increased in both the *Fmr1* KO (n=4, $p = 0.0031$, t-test) and $Cre^{Nex1}/Fmr1^{Flox/y}$ cKO (n=4, $p < 0.0001$, t-test) mice compared to their respective WT counterparts (Table 3; Fig. 4E). As a result, the cleaved aggrecan to total aggrecan ratio was significantly increased in both the *Fmr1* KO (n=4), $p = 0.0003$, t-test) and $Cre^{Nex1}/Fmr1^{Flox/y}$ cKO mice (n=4, $p = 0.0001$, t-test) compared to WT and $Fmr1^{Flox/y}$ mice, respectively (Table 3; Fig. 4F). Our data suggest that loss of FMRP in excitatory neurons contributes to the increased gelatinase activity in adult *Fmr1* KO

and *Cre*^{Nex1}/*Fmr1*$^{Flox/y}$ cKO mouse auditory cortex that may affect formation of WFA+ PNNs around PV interneurons by cleaving aggrecan.

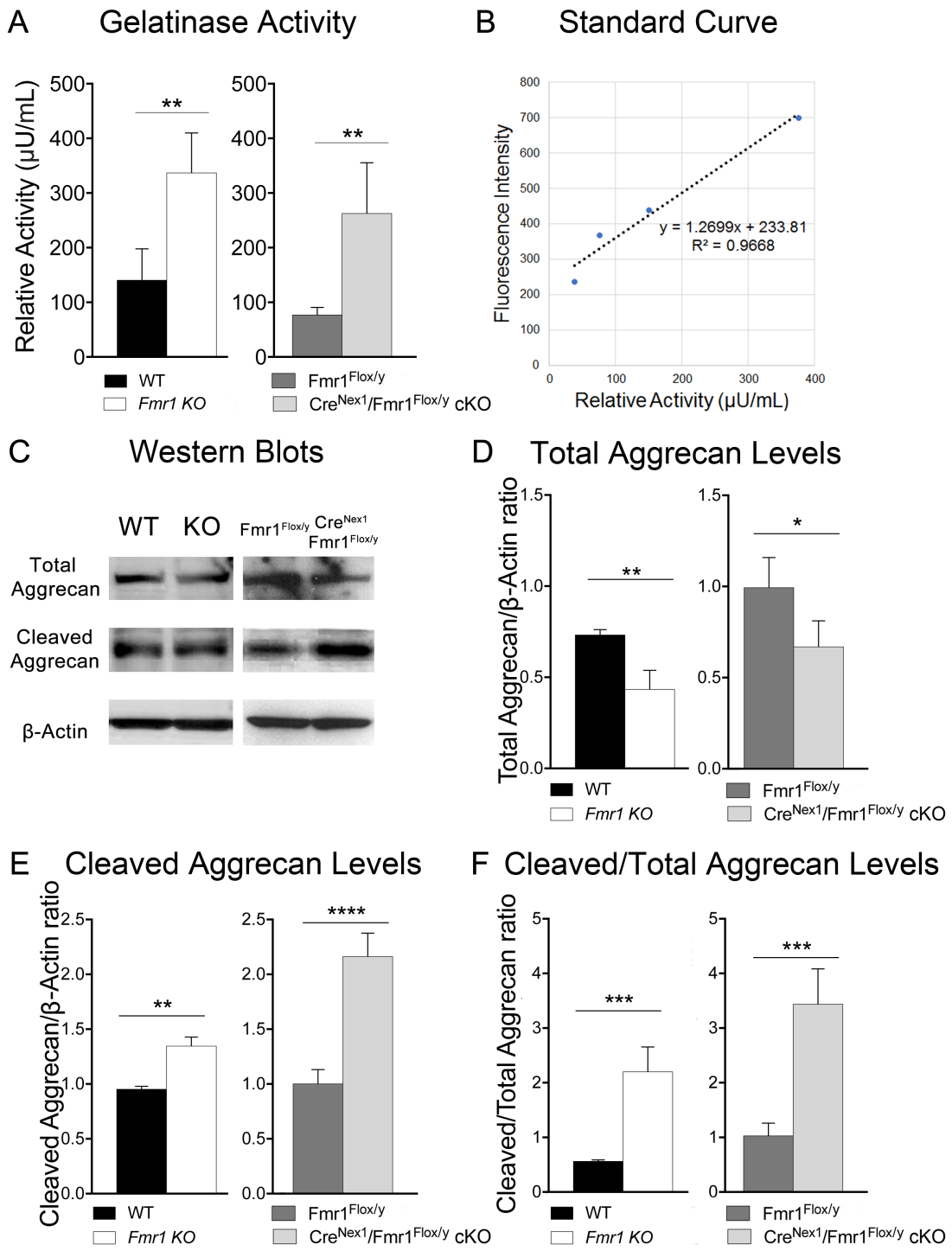

Figure 4. Total aggrecan levels are reduced whereas cleaved aggrecan levels and gelatinase

activity are elevated in the auditory cortex of adult excitatory neuron specific *Cre^{Nex1}/Fmr1$^{Flox/y}$* cKO mice.

(A) Relative gelatinase activity in adult auditory cortex of WT, *Fmr1* KO, *Fmr1*$^{Flox/y}$ and *Cre^{Nex1}/Fmr1$^{Flox/y}$* cKO mice. Graph shows mean ± SEM (n=4/group, **p<0.01, t-test). Gelatinase activity is elevated in *Fmr1* KO and *Cre^{Nex1}/Fmr1$^{Flox/y}$* cKO mice as compared to WT and *Fmr1*$^{Flox/y}$ mice, respectively. (B) Standard curve showing gelatinase activity of recombinant MMP-9. Linear regression graph represents mean ± SEM (n=5). (C) Western blots showing total and cleaved forms of aggrecan. (D-F) Graphs show mean ± SEM (n=4/group, *p<0.05; **p<0.01; ***p<0.001; ****p<0.0001, t-test). Total aggrecan levels were significantly reduced in both the *Fmr1* KO and *Cre^{Nex1}/Fmr1$^{Flox/y}$* cKO mice compared to WT and *Fmr1*$^{Flox/y}$ mice (D). In contrast, cleaved aggrecan levels were significantly increased in the auditory cortex of both *Fmr1* KO and *Cre^{Nex1}/Fmr1$^{Flox/y}$* cKO mice compared to their WT counterparts (E). Cleaved aggrecan to total aggrecan ratio was significantly increased in both the *Fmr1* KO and *Cre^{Nex1}/Fmr1$^{Flox/y}$* cKO mice compared to WT and *Fmr1*$^{Flox/y}$ mice, respectively (F).

Deletion of FMRP from excitatory neurons triggers a decrease in PV levels, while Akt and mTOR phosphorylation is increased in auditory cortex of adult *Cre^{Nex1}/Fmr1$^{Flox/y}$* cKO mice

Consistent with the reduced PV cell density in adult *Fmr1* KO and *Cre^{Nex1}/Fmr1$^{Flox/y}$* cKO mice compared to their controls, we observed a significant decrease in PV levels in the cell lysates from auditory cortex of both *Fmr1* KO (n=4, $p < 0.0001$, t-test) and *Cre^{Nex1}/Fmr1$^{Flox/y}$* cKO mice (n=4, $p = 0.0032$, t-test) compared to their WT counterparts (Table 3; Fig. 5A, D).

642 This is consistent with previous findings that show a reduction in PV expression in cortex of
643 mouse models of autism (Filice et al. 2016).

644 Enhanced Akt/mTOR signaling may also underlie changes in synaptic functions and
645 hyperexcitability associated with FXS and other autistic spectrum disorders (Klann and Dever
646 2004; Sharma et al. 2010; Enriquez-Barreto and Morales 2016; Sato 2016). Therefore, we
647 investigated Akt/mTOR activation in adult auditory cortex of global *Fmr1* KO and forebrain
648 excitatory neuron-specific $Cre^{Nex1}/Fmr1^{Flox/y}$ cKO mice, by examining mTOR and Akt
649 phosphorylation levels (Table 3; Fig. 5B, C). Higher levels of the phosphorylated (i.e., active)
650 forms of both proteins were detected in the adult auditory cortex of *Fmr1* KO mice compared to
651 WT. Specifically, there was a 33% increase in the p-mTOR/mTOR ratio in the *Fmr1* KO mice
652 (n=4, $p = 0.0005$, t-test) compared to WT (Table 3; Fig. 5E). A similar effect was also seen for
653 the p-Akt/Akt ratio, which was 35% higher in the *Fmr1* KO mice (n=4, $p = 0.0051$, t-test)
654 compared to WT mice (Table 3; Fig. 5F). Similar deficits were seen in the auditory cortex of
655 adult $Cre^{Nex1}/Fmr1^{Flox/y}$ cKO mice compared to control $Fmr1^{Flox/y}$ mice. There was a 30%
656 increase in the p-mTOR/mTOR ratio (n=4, $p = 0.0073$, t-test; Table 3; Fig. 5E) and a 40%
657 increase in the p-Akt/Akt ratio in the $Cre^{Nex1}/Fmr1^{Flox/y}$ cKO mice (n=4, $p = 0.0002$, t-test; Table
658 3; Fig. 5F) compared to $Fmr1^{Flox/y}$ mice. These results demonstrate that FMRP deletion from
659 forebrain excitatory neurons is sufficient to trigger enhanced Akt and mTOR phosphorylation in
660 the auditory cortex of adult mice.

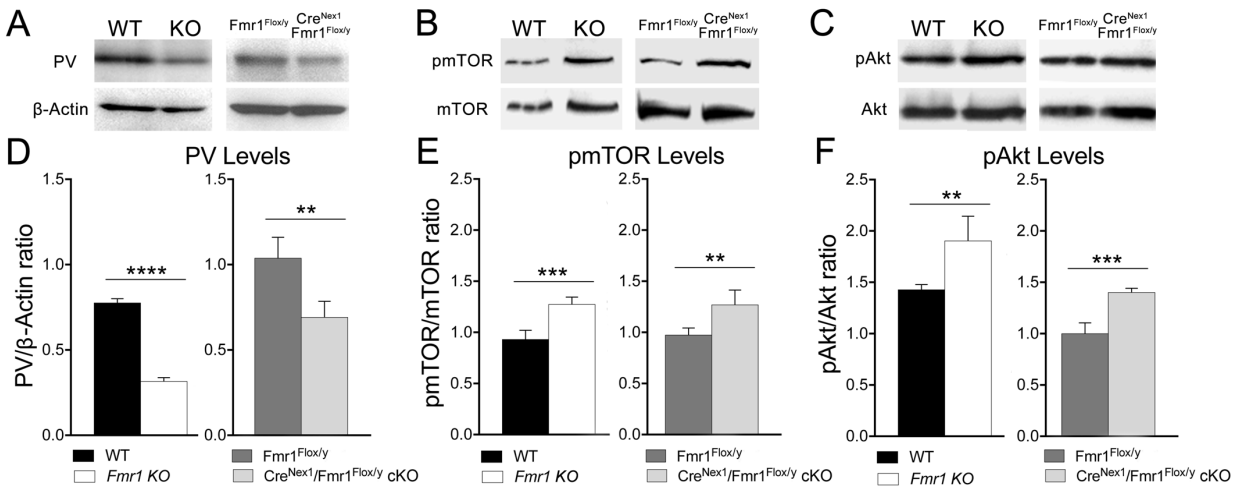

Figure 5. FMRP deletion from forebrain excitatory neurons is sufficient to decrease PV levels and trigger enhanced Akt and mTOR phosphorylation in the auditory cortex of adult mice.

(A-C) Western blot showing PV (A), p-mTOR, mTOR (B), p-Akt and Akt (C) levels in lysates from adult auditory cortex of WT, *Fmr1* KO, *Fmr1*$^{Flox/y}$ and *Cre*^{Nex1}*/Fmr1*$^{Flox/y}$ cKO mice. (D) Quantitative analysis of PV levels. Graphs show mean ± SEM (n=4/group, **p<0.01; ****p<0.0001, t-test). PV levels are significantly reduced in adult auditory cortex of both *Fmr1* KO and *Cre*^{Nex1}*/Fmr1*$^{Flox/y}$ cKO mice compared to their WT counterparts. (E-F) Quantitative analysis of p-mTOR/mTOR (E) and p-Akt/Akt ratios. Graphs show mean ± SEM (n=4/group, **p<0.01; ***p<0.001, t-test). There is a significant increase in the p-mTOR/mTOR ratio in the *Fmr1* KO mice compared to WT (E). There is also a significant increase in the p-Akt/Akt ratio in the *Fmr1* KO mice compared to WT mice (F). Similarly, there is a significant increase in the p-mTOR/mTOR ratio (E) and p-Akt/Akt ratio (F) in the adult auditory cortex of *Cre*^{Nex1}*/Fmr1*$^{Flox/y}$ cKO mice compared to *Fmr1*$^{Flox/y}$ mice.

677 **Table 3.** Gelatinase activity and protein levels in the auditory cortex of adult WT, *Fmr1* KO,

678 *Fmr1*$^{Flox/y}$, and *Cre*^{Nex1}/*Fmr1*$^{Flox/y}$ cKO mice (mean ± SEM).

	WT	*Fmr1* KO	*Fmr1*$^{Flox/y}$	Cre^{Nex1}/*Fmr1*$^{Flox/y}$ cKO
Gelatinase Activity	140.9 ± 28.49	337.4 ± 36.24	77.24 ± 6.71	263.1 ± 46.13
Full-length Aggrecan Levels	0.7252 ± 0.0141	0.4346 ± 0.0516	0.992 ± 0.0667	0.6692 ± 0.0705
Cleaved Aggrecan Levels	0.9546 ± 0.0217	1.347 ± 0.0399	1.004 ± 0.0742	2.142 ± 0.0847
Cleaved/Total Aggrecan ratio	0.5653 ± 0.0107	2.205 ± 0.2258	0.9916 ± 0.1016	3.524 ± 0.2743
PV Levels	0.7768 ± 0.0096	0.3176 ± 0.0103	1.022 ± 0.0522	0.6918 ± 0.0467
p-mTOR/mTOR ratio	0.9333 ± 0.0359	1.275 ± 0.0343	0.963 ± 0.030	1.271 ± 0.072
p-Akt/Akt ratio	1.362 ± 0.0434	1.906 ± 0.1187	0.9699 ± 0.052	1.403 ± 0.0196

679

680 **Resting EEG gamma power is enhanced in the auditory cortex of adult *Cre*^{Nex1}/*Fmr1*$^{Flox/y}$**

681 **cKO mice**

682 If impaired formation of WFA+ PNNs around PV interneurons and enhanced gelatinase

683 activity in the auditory cortex underlie abnormal neural oscillations observed in the global *Fmr1*

684 KO mice (Wen et al. 2018; Lovelace et.al. 2018), then we should see similar deficits in forebrain

685 excitatory neuron-specific *Cre*^{Nex1}/*Fmr1*$^{Flox/y}$ cKO mice. However, it is also possible that some

686 of these electrophysiological deficits are inherited from loss of FMRP from other cell-types or

687 subcortical sites (Strumbos et al. 2010; Beebe et al. 2014; Wang et al. 2014; Rotschafer et al.

688 2015; Garcia-Pino et al. 2017). Therefore, we quantified EEG responses in *Cre*^{Nex1}/*Fmr1*$^{Flox/y}$

689 cKO mice.

690 Baseline EEG raw power was calculated in auditory cortex of control *Fmr1*$^{Flox/y}$ (n=9)

691 and *Cre*^{Nex1}/*Fmr1*$^{Flox/y}$ cKO (n=9) mice by analyzing all frequency bands during the entire 5min

resting period. Examples of 1sec segments of resting EEG for each genotype, as well as genotype averages (+/- SEM) of power spectra are depicted in Fig. 6. Even in the raw traces (Fig. 6A), enhanced high frequency oscillations are apparent in auditory cortex. The group average power spectral densities are shown in Fig. 6B, wherein genotype differences in auditory cortex can be seen at frequencies ~40Hz (Fig. 6B). Statistical analysis was performed using a one-way MANCOVA approach with percentage time spent moving as a covariate. We compared genotype mean differences on 6 bands per region: Delta (1-4Hz), Theta (4-10Hz), Alpha (10-13Hz), Beta (13-30Hz), Low Gamma (30-55Hz), and High Gamma (65-100Hz). The gamma band (30-100 Hz) was divided because multiple studies suggest that low (30-60 Hz) versus high frequency (>60 Hz) bands in gamma range may arise from different mechanisms (Ray and Maunsell 2011; Balakrishnan and Pearce 2014; Dvorak and Fenton 2014). Using this approach, we confirmed assumptions of equality of covariance using Box's M, $p = 0.089$, as well as Levene's test of equality of error variance, no differences between genotypes were observed in error variance (all $p>0.05$). Since assumptions were not violated, we report an effect of genotype (Pillai's Trace = 0.738, $p = 0.016$) across all 6 of the combined frequency variables, which include movement as a covariate. We then determined that the only individual frequency band difference between genotypes in the auditory cortex of $Cre^{Nex1}/Fmr1^{Flox/y}$ cKO mice was in the low gamma band (Fig. 6C, D). Low gamma was significantly increased after correction for multiple comparisons: auditory cortex low gamma, $F(1,15) = 12.258$, $p = 0.0032$, $\eta^2 = 0.45$. These data lead to the interpretation that the auditory cortex low gamma differences in the global *Fmr1* KO mice likely arises due to local circuit defects. Gamma power is influenced, at least in part, by PV+ interneuron function in the cortex (Sohal et al., 2009). Observed increased

gelatinase activity along with reduced PV+ cell density and WFA+ PNNs around PV+ neurons is likely involved in the local circuit dysfunction and increased low gamma power reported here.

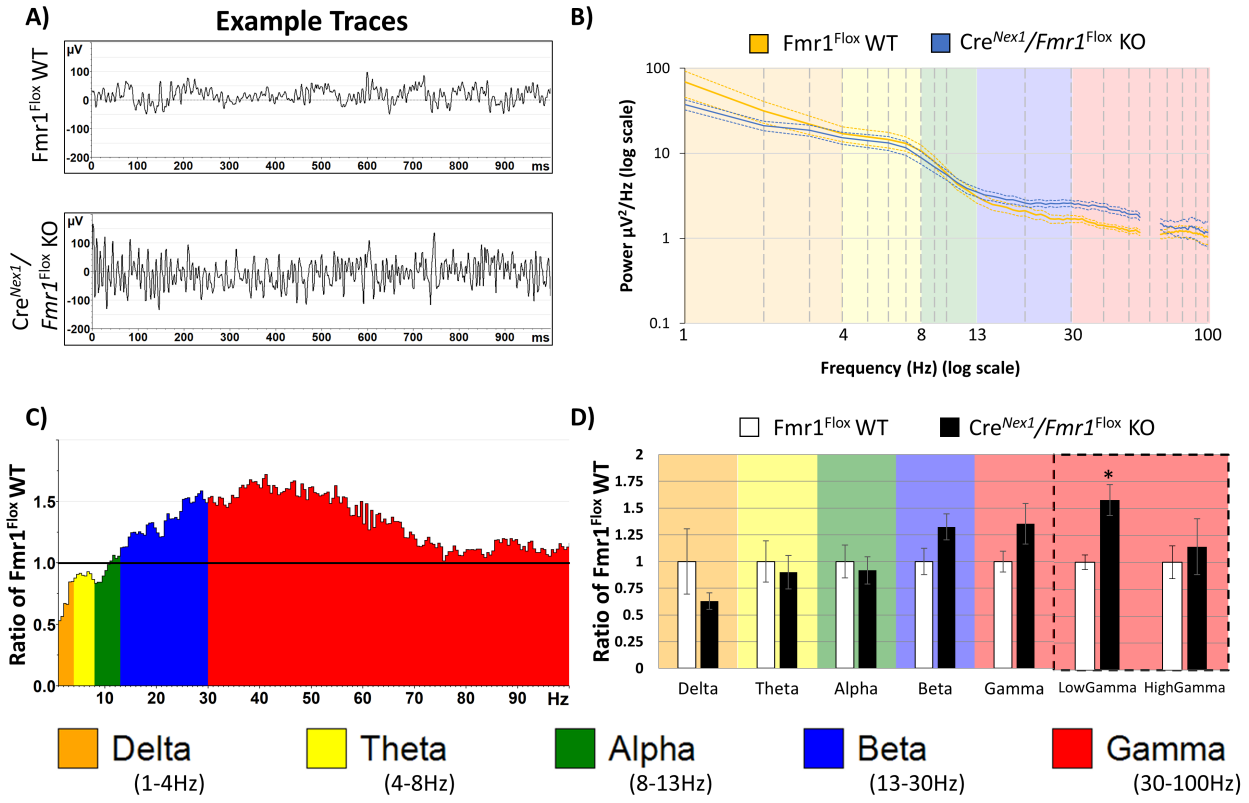

Figure 6. Forebrain excitatory neuron specific deletion of *Fmr1* reveals increased Low Gamma Power in auditory cortex of adult mice.

Five minutes of baseline EEG data (in the absence of auditory stimulation) from electrodes implanted in the auditory cortex of *Fmr1*$^{Flox/y}$ (n=9) and *Cre*^{Nex1}/*Fmr1*$^{Flox/y}$ cKO mice (n=9) was recorded and FFT analysis was done to determine spectral power. (A) Depicted are examples of such segments from control *Fmr1*$^{Flox/y}$ (A, top) and *Cre*^{Nex1}/*Fmr1*$^{Flox/y}$ cKO (A, bottom) mice mouse auditory cortex. (B) Power density (μV^2/Hz) was calculated for each artifact-free segment using Fast Fourier Transform, followed by averaging of all segments for a given mouse. These individual averages then contributed to the genotype grand average for each genotype (n=9 per genotype). Significant differences between genotypes are observed in auditory cortex at

low gamma Frequencies (30-55Hz). Note: frequencies from 55-65Hz were excluded in *all* analysis, as a 60Hz notch filter was utilized to eliminate line noise.**(C)** Average power in the *Cre*^{Nex1}/*Fmr1*$^{Flox/y}$ cKO mouse auditory cortex is expressed as the ratio of control levels (*Fmr1*$^{Flox/y}$). A value of 1 (horizontal black line) indicates no mean difference in power at that frequency between genotypes while values above the black line indicate *Cre*^{Nex1}/*Fmr1*$^{Flox/y}$ cKO > *Fmr1*$^{Flox/y}$, and below the black line indicates *Cre*^{Nex1}/*Fmr1*$^{Flox/y}$ cKO < *Fmr1*$^{Flox/y}$. **(D)** Auditory cortex values were divided into standard frequency bands. MANCOVA analysis controlling for the effect of movement, revealed differences in the low gamma range of auditory cortex after Bonferroni correction for multiple comparisons. *p<0.05.

Gamma synchronization is not affected in adult *Cre*^{Nex1}/*Fmr1*$^{Flox/y}$ cKO mouse auditory cortex

We hypothesized that the increased baseline gamma in *Cre*^{Nex1}/*Fmr1*$^{Flox/y}$ cKO mouse auditory cortex would lead to a deficit in generating consistent phase locking in gamma frequencies across trials. This is because the observed increased gamma power during rest (no auditory stimulation) may act as "noise" and interfere with consistency of sound-evoked responses from trial to trial. Both up and down chirps were tested to ensure that the differences are specific to modulation frequencies and are not affected by the direction of frequency change in the sound. Briefly, a 'chirp' stimulus is a broadband noise, which is amplitude modulated over the course of its duration (2s). The rate of modulation either goes from 100Hz down to 1Hz over 2s (down chirp) or goes from 1Hz up to 100Hz over 2s (up chirp, see Figure 7, bottom). After repeated chirp presentation (300 trials for up, 300 for down), the inter trial phase coherence (ITPC) was calculated across trials in the time X frequency domain using Morlet Wavelet

analysis, similar to our previously published results (Lovelace et al. 2018). After grand average ITPC was calculated for each group, means for *Fmr1*$^{Flox/y}$ mice (n=9) were subtracted from the means for *Cre*^{Nex1}*/Fmr1*$^{Flox/y}$ cKO (n=9) (Fig. 7A, only 'up' chirp data are shown). For statistical comparisons, non-parametric cluster analysis was used to determine contiguous regions in the time X frequency domain that were statistically different between genotypes (Fig. 7A). We observed no significant differences in gamma band ITPC in the auditory cortex of *Cre*^{Nex1}*/Fmr1*$^{Flox/y}$ cKO mice (Fig. 7A). Similar patterns and statistics of ITPC were observed for both up and down chirps (down chirp data not shown). These data show that the gamma synchronization deficits observed in the global *Fmr1* KO mouse auditory cortex are not due to abnormal expression of FMRP in forebrain excitatory neurons. Either other cell types in the cortex are specifically involved in the consistency of phasic responses to amplitude-modulated noise (ex. FMRP expressed in astrocytes or GABAergic neurons), or the ITPC deficit found in the global *Fmr1* KO is inherited from subcortical sites wherein neurons phase lock to faster amplitude modulation rates than the cortex.

Increased non-phase locked single trial power is observed in the auditory cortex of adult *Cre*^{Nex1}*/Fmr1*$^{Flox/y}$ cKO mice during chirp stimulation

We investigated non-phase locked Single Trial Power (STP) during the chirp stimulation period (Fig. 7B) because we previously reported a significant increase in STP in the global *Fmr1* KO mouse. An increase in STP is also seen in humans with FXS (Ethridge et al. 2017). Using the same statistical cluster analysis as for the chirp ITPC, the *Cre*^{Nex1}*/Fmr1*$^{Flox/y}$ cKO mice showed an increase in background gamma power in the auditory cortex and only in the lower gamma band (Fig. 7B). These data suggest that low-gamma deficits in non-phase locked power

in the auditory cortex is due to deficits in local circuits mediated by abnormal FMRP in cortical excitatory neurons. This also suggests that the low gamma power increase during silence (Fig. 6 resting EEG data) is still present throughout sound presentation.

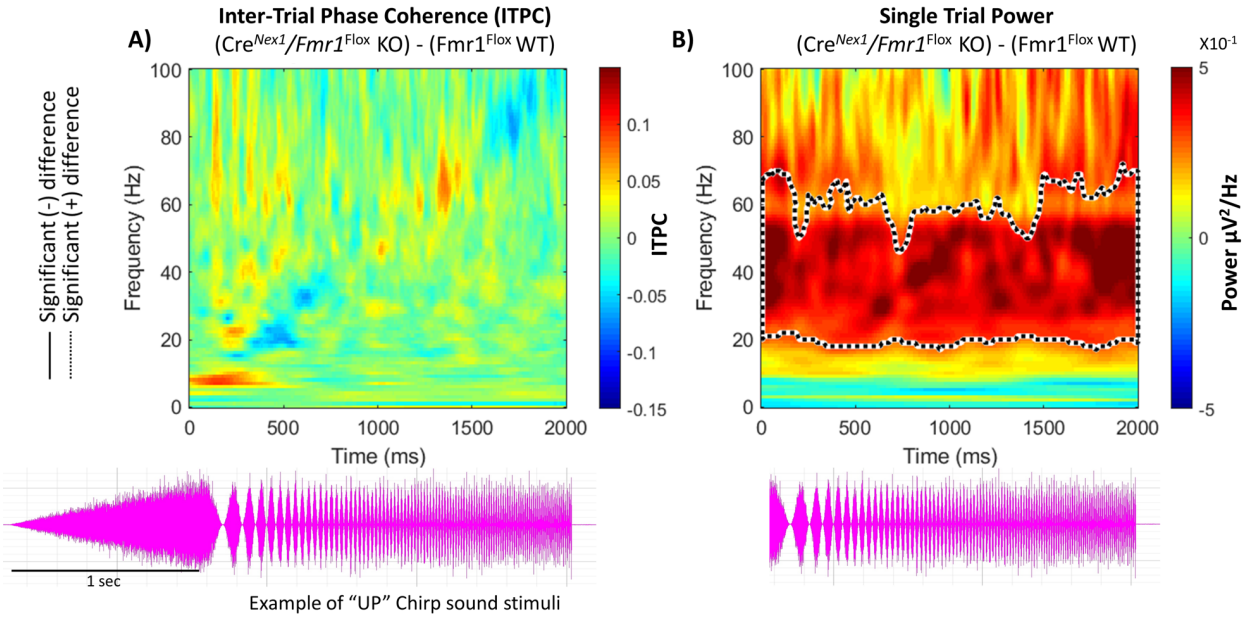

Figure 7. Adult *Cre^{Nex1}/Fmr1$^{Flox/y}$* cKO mice show no phenotype in Phase Locking to Auditory "Up Chirp" stimuli, but non-phase locked single trial power was enhanced.

(A) Trains of chirp modulated broadband noise (bottom) were presented to each mouse 300 times. For each mouse, inter-trial phase coherence (ITPC) was measured to determine the degree of phase locking across trials. Grand average matrices were calculated for each genotype, and then *Fmr1*$^{Flox/y}$ (n=9) ITPC values were subtracted from *Cre^{Nex1}/Fmr1$^{Flox/y}$* cKO (n=9) values. Blue areas indicating *Cre^{Nex1}/Fmr1$^{Flox/y}$* cKO < *Fmr1*$^{Flox/y}$, green areas no difference, and red *Cre^{Nex1}/Fmr1$^{Flox/y}$* cKO > *Fmr1*$^{Flox/y}$. Statistical cluster analysis reveals contiguous time x frequency regions that are significantly different between genotypes. Black solid contours (mean negative group difference) and black dashed contours (mean positive group difference) indicate these significant clusters. After subtraction and cluster analysis in auditory cortex, *Cre^{Nex1}/Fmr1$^{Flox/y}$* cKO mice express no statistically significant changes in ITPC along the

diagonal band elicited by the Up Chirp . **(B)** For each mouse, single-trial power (STP) was measured to determine the average total non-phase locked power during sound presentation. Grand average matrices were calculated for each genotype, and then *Fmr1*$^{Flox/y}$ (n=9) STP values were subtracted from *Cre*^{Nex1}*/Fmr1*$^{Flox/y}$ cKO (n=9) values. Blue areas indicating *Cre*^{Nex1}*/Fmr1*$^{Flox/y}$ cKO < *Fmr1*$^{Flox/y}$, green areas no difference, and red *Cre*^{Nex1}*/Fmr1*$^{Flox/y}$ cKO > *Fmr1*$^{Flox/y}$. Statistical cluster analysis reveals contiguous time x frequency regions that are significantly different between genotypes. Black dashed contour indicate these significant clusters. After subtraction and cluster analysis in auditory cortex, *Cre*^{Nex1}*/Fmr1*$^{Flox/y}$ cKO mice express statistically significant increase in STP throughout the sound presentation in the low gamma range (~20-60Hz), consistent with resting EEG analysis.

Induced power is significantly enhanced in the auditory cortex of adult *Cre*^{Nex1}*/Fmr1*$^{Flox/y}$ cKO mice

In addition to phase locking to the auditory chirp, we also compared genotypes on auditory cortex responses to 100 trains of brief broadband noise stimulus (100ms each noise burst, 10 stimuli per train). We tested both a habituating rate of presentation (4Hz) and a non-habituating rate (0.25Hz) (Lovelace et.al. 2016). Example traces of single sound presentation for both genotypes are shown in Fig. 8A and the first 4 stimuli in the 4Hz train in Fig. 8D. We measured both ITPC and induced power (baseline corrected non-phase locked single trial power) for each repetition rate. First, the ITPC for the non-habituation 0.25Hz rate showed a reduction in phase locking in the beta range (~20-30Hz) immediately after sound presentation (Fig. 8B). This suggests that *Cre*^{Nex1}*/Fmr1*$^{Flox/y}$ cKO mice are more variable in their ERP latencies compared to control *Fmr1*$^{Flox/y}$ mice at those specific frequencies. In addition, *Cre*^{Nex1}*/Fmr1*$^{Flox/y}$ cKO mice

displayed an increase in induced power ~100ms following the onset of the sound from the beta to low gamma range (~10-50Hz) (Fig. 8C). This result is indicative of increased "on-going" response after the initial onset ERP (Rotschafer and Razak 2013). Using the same analysis on the first 4 responses to a 4Hz train of sounds reveals the same ITPC deficit for the first sound in the train (reduction in ITPC from ~20-30Hz), with no difference during the rest of the train (Fig. 8E). However, after repeated sound stimulation, the on-going non-phase locked power persists throughout the entire train presentation (Fig. 8F). This effect is visually apparent in the example traces shown in Fig. 8D, where the $Cre^{Nex1}/Fmr1^{Flox/y}$ cKO mouse shows persistent high frequency oscillations throughout the sound train, while the control $Fmr1^{Flox/y}$ mouse is relatively quiet. These combined results indicate that the variability of latencies to the onset of sound is increased (reduction in ITPC) when FMRP is removed from excitatory cortical neurons, and suppression of on-going activity is reduced in the auditory cortex both after single sound presentation and repeated presentations.

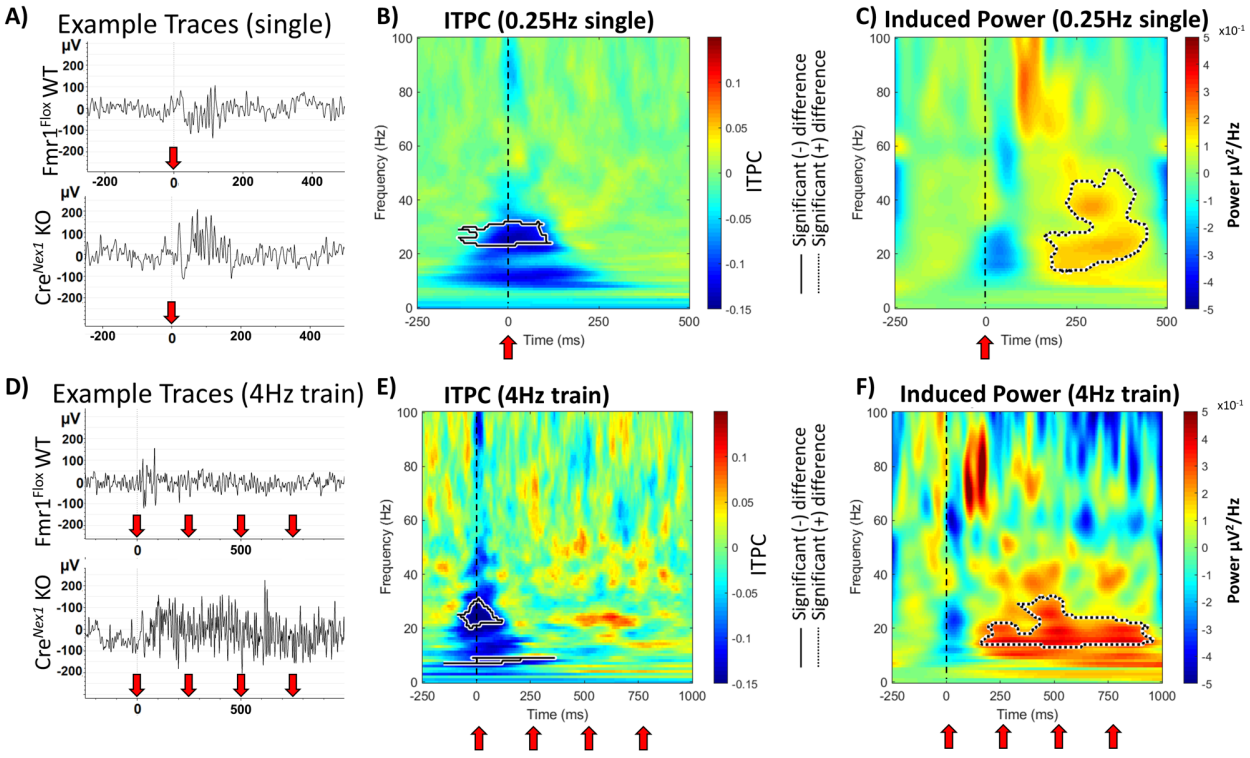

Figure 8. Increase in induced (non-phase locked) power is seen in adult *Cre^{Nex1}/Fmr1$^{Flox/y}$* cKO mice.

(A) Example traces in response to single sound presentations at 0.25Hz from both genotypes. Red arrow indicates onset of 100ms broadband noise. (B) Grand average difference plot of inter trial phase coherence (ITPC) during single sound presentations between genotypes (*Cre^{Nex1}/Fmr1$^{Flox/y}$* cKO - *Fmr1*$^{Flox/y}$). There is a reduction in ITPC in the *Cre^{Nex1}/Fmr1$^{Flox/y}$* cKO mice ~20-30Hz immediately after sound presentation. (C) Baseline corrected single trial power (induced power) was calculated for each genotype and difference plot is shown. Increased induced power is observed following the initial ERP response, indicating increased "on-going" activity after sound presentation. (D) Examples traces of 4Hz sound presentation for both genotypes, only the first 4 noise bursts of each train were analyzed. (E) ITPC differences were observed for the first sound in the train in the same range as seen in the single response in B, but no differences were seen with subsequent sound presentation at 4Hz. (F) Increased induced

power was observed after the first sound presentation and persisted with subsequent sounds. This effect is also apparent in the example traces in D.

Excitatory neuron specific adult *Cre^{Nex1}/Fmr1$^{Flox/y}$* cKO mice display increased locomotor activity, but no anxiety-like behavior.

Adult male *Fmr1*$^{Flox/y}$ (n=6) and *Cre^{Nex1}/Fmr1$^{Flox/y}$* cKO (n=6) mice were tested for locomotor activity and anxiety in an elevated plus maze by measuring total number of entries or speed and time spent in open arms, respectively (Table 4; Fig. 9). *Cre^{Nex1}/Fmr1$^{Flox/y}$* cKO mice demonstrated an increased locomotor activity by making significantly more total arm entries than *Fmr1*$^{Flox/y}$ mice (n=6, $p = 0.0262$, t-test) (Table 4; Fig. 9A), and by showing a significant increase in speed (n=6, $p = 0.0063$, t-test) (Table 4; Fig. 9B). However, *Cre^{Nex1}/Fmr1$^{Flox/y}$* cKO mice showed no difference in time spent in open arm per entry (n=6, $p = 0.2731$, t-test) or percentage of time in open arms (n=6, $p = 0.0521$, t-test) compared to *Fmr1*$^{Flox/y}$ mice (Table 4; Fig. 9C-D).

We used an open-field test as another gauge of locomotor activity and anxiety, by determining total number of lines crosses or speed and the tendency of mice to travel through the center of an open field or the time in thigmotaxis, respectively. Similar to the performance in the elevated plus maze, *Cre^{Nex1}/Fmr1$^{Flox/y}$* cKO mice showed increased locomotor activity with significantly more line crosses (n=6, $p = 0.0014$, t-test) (Table 4; Fig. 9E) and increased speed (n=6, $p = 0.0045$, t-test) (Table 4; Fig. 9F) than *Fmr1*$^{Flox/y}$ mice. However, there was no significant difference in time spent in the center per entry (n=6, $p = 0.8624$, t-test) or percentage of time in thigmotaxis (n=6, $p = 0.1834$, t-test) between the two groups (Table 4; Fig. 9G-H). These findings establish that FMRP deletion from forebrain excitatory neurons increases locomotor activity but has no effect on anxiety-like behaviors.

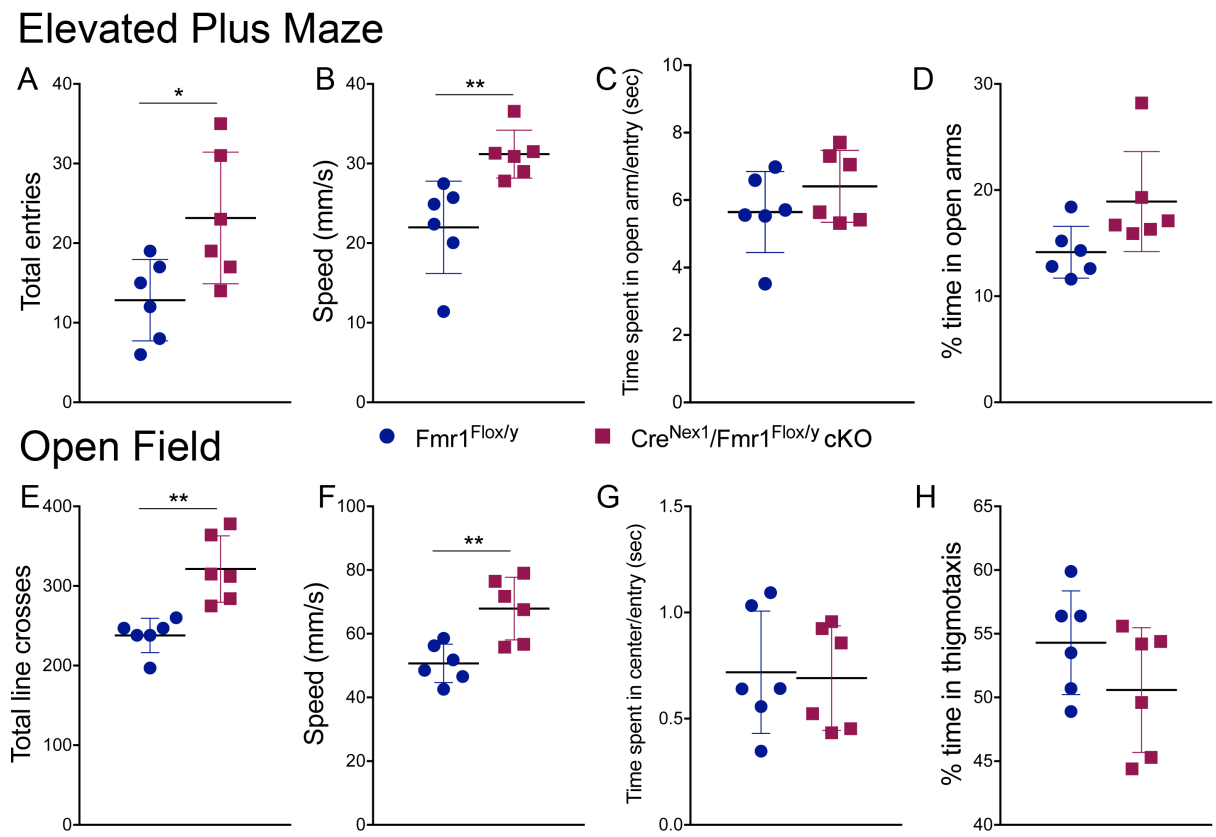

Figure 9. Adult excitatory neuron specific *Cre^{Nex1}/Fmr1$^{Flox/y}$* cKO mice display increased locomotor activity, but no anxiety-like behavior.

(A–D) Graphs demonstrate the performance of *Cre^{Nex1}/Fmr1$^{Flox/y}$* cKO mice in the elevated plus maze as measured by the total number of arm entries (A), speed (B), the total amount of time spent in the open arm per entry (C), and the percent of time spent in the open arms (D). Graphs show mean ± SEM (n=8/group, *p<0.05; **p<0.01, t-test).

(E–H) Graphs demonstrate the performance of *Cre^{Nex1}/Fmr1$^{Flox/y}$* cKO mice in the open field as measured by the total number of line crosses (E), speed (F), the amount of time spent in the center per entry (G), and the percent time spent in thigmotaxis (H). Graphs show mean ± SEM (n=8/group, **p<0.01, t-test).

874 **Table 4.** Locomotor activity and *anxiety* measures of *Fmr1*$^{Flox/y}$ and *Cre*^{Nex1}/*Fmr1*$^{Flox/y}$ cKO mice

875 using elevated plus maze (EP) and open-field (OF) behavior tests (mean ± SEM).

	Fmr1$^{Flox/y}$	Cre^{Nex1}/*Fmr1*$^{Flox/y}$ cKO
Total entries (EP)	12.83 ± 2.088	23.17 ± 3.371
Speed (EP)	21.99 ± 2.37	31.18 ± 1.23
Time spent in open arm/entry (EP)	5.648 ± 0.4904	6.408 ± 0.4348
% Time in open arms (EP)	14.15 ± 0.9986	18.92 ± 1.919
Total line crosses (OF)	237.8 ± 8.807	321.3 ± 17.03
Speed (OF)	50.72 ± 2.462	67.9 ± 4.016
Time spent in center/entry (OF)	0.719 ± 0.1177	0.6914 ± 0.1007
% Time in thigmotaxis (OF)	54.3 ± 1.663	50.58 ± 1.999

876

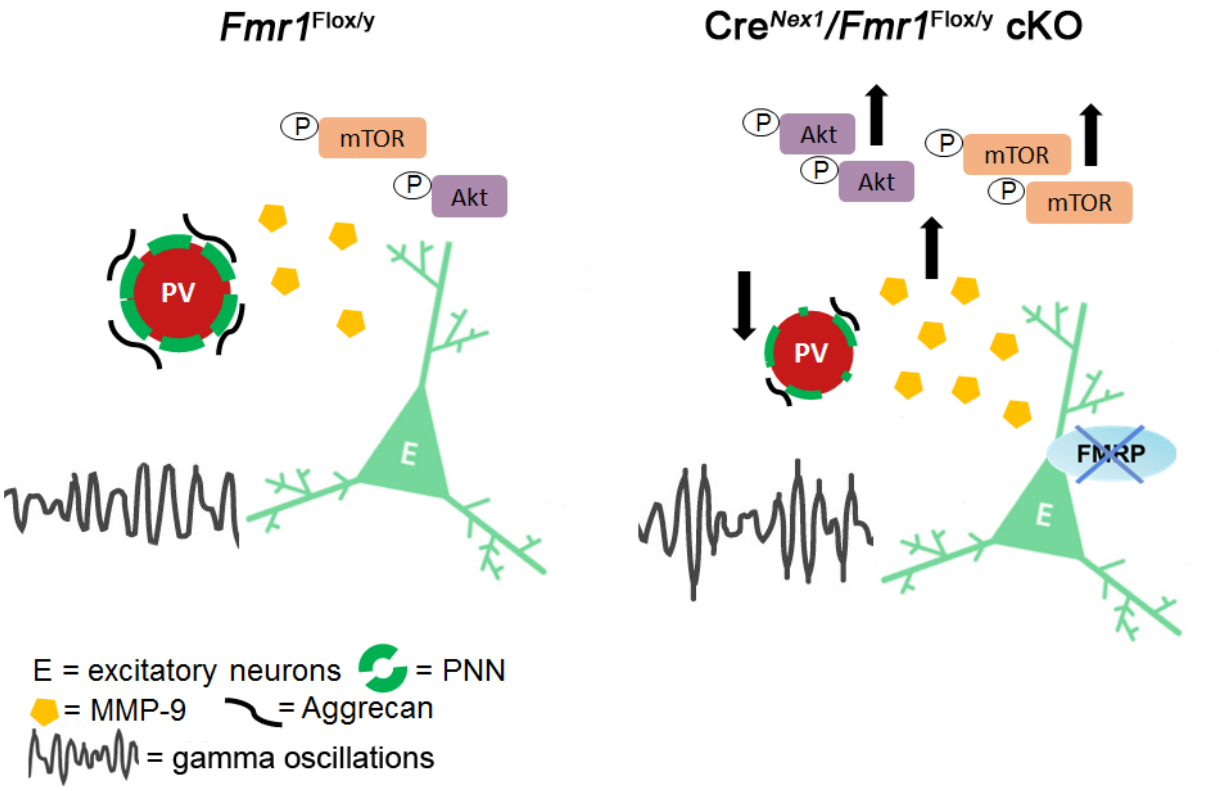

877

878 **Figure 10. Schematic of cellular and EEG phenotypes in the auditory cortex of adult**

879 ***Cre*^{Nex1}*/Fmr1*$^{Flox/y}$ cKO compared to *Fmr1*$^{Flox/y}$ mice.**

880 Left panel depicts normal cellular and EEG phenotypes in the auditory cortex of *Fmr1*$^{Flox/y}$ mice.

881 Right panel depicts reduced PV levels, impaired formation of WFA+ PNNs around PV cells,

882 increased gelatinase activity and mTOR/Akt phosphorylation, and abnormal neural oscillations

883 in auditory cortex of excitatory neuron-specific *Cre*^{Nex1}*/Fmr1*$^{Flox/y}$ cKO mice.

884

885 **Discussion**

886 Sensory processing deficits commonly co-occur with autism spectrum disorders. The

887 mechanisms of sensory deficits in autism remain poorly understood, and no current therapies are

888 available to alleviate sensory symptoms. The main findings of this study provide novel insights

889 into mechanisms of sensory processing issues in FXS, a leading genetic cause of autism

890 (summarized in Fig. 10). We show that cell-type specific deletion of *Fmr1* from forebrain
891 excitatory neurons is sufficient to trigger an abnormal EEG phenotype in the adult auditory
892 cortex, such as increased power of resting low-gamma oscillations. In addition, we show that
893 deletion of *Fmr1* from forebrain excitatory neurons elicits elevated gelatinase activity, higher
894 mTOR/Akt phosphorylation, and impaired PV/PNN colocalization in the auditory cortex. While
895 both astrocytes and neurons can release gelatinases MMP-2 and MMP-9 (Yong et al. 1998;
896 Szklarczyk et al. 2002; Murase et al. 2016), our data suggest that loss of FMRP from excitatory
897 neurons is sufficient to trigger increased gelatinase activity, which may affect the formation of
898 WFA+ PNNs around PV interneurons.
899 Abnormal density and function of PV+ GABAergic interneurons appears to be a common
900 finding across sensory cortices in FXS model mice, and may be a common mechanism for
901 abnormal sensory processing and sensitivity (Selby et al. 2007; Contractor et al. 2015; Goel et al.
902 2018; Wen et al., 2018). PV expression in inhibitory neurons is activity-dependent (Patz et al.
903 2004; Chang et al. 2010). The reduction in PV expression in $Cre^{Nex1}/Fmr1^{Flox/y}$ cKO mouse
904 auditory cortex may occur due to reduced excitatory drive onto these neurons. *In vitro* slice
905 physiology studies of somatosensory cortex in global *Fmr1* KO mice have shown local circuit
906 deficits with reduced excitatory input received by PV interneurons, whereas excitatory and
907 inhibitory drive onto excitatory neurons was normal (Gibson et al. 2008). Consistent with our
908 data, these deficits are seen following removal of FMRP just from excitatory neurons suggesting
909 that a common mechanism across sensory cortices in *Fmr1* KO mice is reduced excitation of PV
910 cells (Selby et al. 2007; Contractor et al. 2015; Goel et al. 2018). A second reason for altered PV
911 cell function might be through the degradation of aggrecan-containing WFA+ PNNs. In the
912 cerebral cortex, PNN loss around PV cells reduces excitability of these cells (Balmer 2016;

913 Lensjø et al. 2017; Wen et al. 2018). Therefore, degradation of PNN is predicted to decrease
914 excitability of PV cells leading to hyperexcitability of cortical networks and abnormal neural
915 oscillations. PNNs protect PV cells from oxidative stress, and the loss of PNNs may lead to PV
916 cell death (Cabungcal et al., 2013).

917 The decrease in PV cell number and function is predicted to have major implications for
918 processing of auditory input in the cortex and may, at least partially, underlie auditory
919 hypersensitivity. PV+ neurons comprise nearly 50% of all GABAergic cells in the neocortex,
920 and individual PV+ neurons can provide synchronized inhibition on to multiple pyramidal cells
921 contributing to network activity levels and patterns (Packer and Yuste, 2011). PV+ neurons are
922 involved in gain control in the auditory cortex, and shape how neurons respond to increasing
923 sound levels (Moore and Wehr, 2013), suggesting a possible neural correlate of abnormal
924 auditory sensitivity. Reduction of PV expression causes GABA neuron dysfunction and
925 facilitation in response to repetitive stimulation, particularly at gamma frequencies (Lucas et al.,
926 2010). Rapid spiking, putative, PV+ cells are also linked to processing of rapid spectrotemporal
927 changes in acoustic inputs (Atencio and Schreiner, 2008) and may be linked to the reduced
928 selectivity for frequency modulated sweep rates in *Fmr1* KO mouse auditory cortex (Rotschafer
929 and Razak, 2013). Cortical gamma oscillations are linked to the function of PV+ interneurons
930 (Gonzalez-Burgos and Lewis 2008; Cardin et al. 2009; Sohal et al. 2009; Volman et al. 2011;
931 Carlén et al. 2012; Keeley et al. 2017). Gamma band activity is involved in a broad array of
932 sensory and cognitive processes, several of which are affected in FXS. The gamma phase-
933 locking deficits may cause sensory discrimination deficits (Cardin et al., 2009; Sohal et al., 2009)
934 that may lead to delayed language and cognitive development in FXS. Low frequency

935 oscillations are involved in attention processes and can modulate high-frequency oscillations,
936 which can be abnormal in *Fmr1* KO mice (Radwan et al., 2016).

937 Our finding of correlated reduction in PV/PNN density and increase in low-gamma
938 power may, at least at the superficial level, seem inconsistent with studies that suggest PV cell
939 activity increases gamma oscillations (Sohal et al. 2009). However, a number of recent studies
940 have suggested that the relationship between interneuron activity and oscillations is complex,
941 and include disinhibitory and compensatory mechanisms (Tsodyks et al. 1997; Ozeki et al.
942 2009). For example, decreased excitatory drive onto PV interneurons in a Schizophrenia model
943 resulted in increased gamma oscillations, and interestingly, increased locomotor activity (Del
944 Pino et al. 2013). Acute rhythmic stimulation of PV cells using optogenetics *in vivo* can generate
945 neural oscillations at gamma frequencies, but not at other frequencies (Cardin et al. 2009).
946 However, somatostatin (SOM) interneurons are also shown to be critical for stimulus-induced
947 gamma rhythms in the visual cortex (Veit et al. 2017). While both PV and SOM interneurons
948 contribute to gamma oscillations, it is possible that prolonged loss of PV cells may trigger an
949 increase in somatostatin interneuron firing and synchronized gamma oscillations to compensate
950 for the change in E-I balance reflecting homeostatic stabilization of the circuits (Antoine et al.
951 2019).

952 Within the broadband gamma oscillations (30-100 Hz) only the low gamma band power
953 is increased in the auditory cortex of $Cre^{Nex1}/Fmr1^{Flox/y}$ cKO mice. The differential effects on
954 gamma frequencies are consistent with multiple studies suggesting different mechanisms
955 responsible for generating low gamma (~30-60 Hz) and high gamma (60-120 Hz) (Ray and
956 Maunsell 2011; Balakrishnan and Pearce 2014; Dvorak and Fenton 2014). Ray and Maunsell
957 (2011) suggested that the low gamma band reflects true oscillations that arise through PV neuron

958 firing and synchronization of pyramidal cell activity, whereas the higher gamma frequencies
959 reflect irregular spiking activity near the electrodes.
960 FMRP is expressed in multiple regions of the auditory pathway (Zorio et al. 2017).
961 Abnormal auditory processing and plasticity have been reported in the brainstem (Chen and Toth
962 2001; Strumbos et al. 2010; Wang et al. 2014; Rotschafer et al. 2015) and auditory cortex (Kim
963 et al. 2013; Rotschafer and Razak 2013; Lovelace et al. 2016; Sinclair et al. 2017; Lovelace et al.
964 2018) of global *Fmr1* KO mice. The abnormal responses seen in the cortex may be inherited
965 from deficits in subcortical sites and/or created *de novo* due to local cortical circuit deficits. Our
966 data show that *Fmr1* deletion in forebrain excitatory neuron is sufficient to elicit enhanced
967 resting low-frequency gamma power in the auditory cortex. However, resting EEG high-gamma
968 power and chirp-elicited phase locking factor were relatively normal in the $Cre^{Nex1}/Fmr1^{Flox/y}$
969 cKO mice. Together, these data suggest that both cortical and sub-cortical structures contributes
970 to changes in physiological responses observed in the auditory cortex of *Fmr1* KO mice.
971 Because the auditory system consists of a number of feed-forward and feedback loops, potential
972 for non-linear interactions in terms of cortical deficits influencing sub-cortical processing cannot
973 be discounted. To begin gaining a systems-level understanding of sensory deficits in autism,
974 future studies will address the effects of *Fmr1* deletion in other cortical cell types and brain
975 areas. Global *Fmr1* KO mice in which *Fmr1* is specifically re-expressed only in the forebrain
976 excitatory neurons, and mouse models in which *Fmr1* is specifically deleted in inhibitory
977 neurons, astrocytes or auditory brainstem would help to shed light on the underlying circuit level
978 mechanisms.
979 *Role of enhanced gelatinase activity in* $Cre^{Nex1}/Fmr1^{Flox/y}$ cKO *mice*

PNNs are comprised of hyaluronan, glycoproteins, and chondroitin sulfate proteoglycans (CSPGs), and form a net-like structure on the cell body and proximal dendrites of PV-expressing GABAergic interneurons. Among CSPGs present in PNNs, aggrecan is found almost exclusively in PNNs formed around PV cells (McRae et al. 2007; McRae et al. 2010; Morawski et al. 2012), and excessive proteolytic activity of gelatinases MMP-2 and MMP-9 may affect formation of PNNs and PV functions by cleaving aggrecan (d'Ortho et al. 1997). Indeed in our studies we observed enhanced gelatinase activity and increased cleavage of aggrecan in the auditory cortex of $Cre^{Nex1}/Fmr1^{Flox/y}$ cKO mice. Consistent with our previous studies in the developing auditory cortex of global *Fmr1* KO mice (Wen et al. 2018), we found that gelatinase activity was also significantly increased in the adult auditory cortex of both *Fmr1* KO and $Cre^{Nex1}/Fmr1^{Flox/y}$ cKO mice, suggesting that the deletion of FMRP from excitatory neurons is sufficient to increase gelatinase activity in the auditory cortex. Our studies suggest that aggrecan cleavage by MMP-9 is likely responsible for impaired formation of WFA+ PNNs around PV interneurons observed in adult auditory cortex of forebrain excitatory neuron-specific $Cre^{Nex1}/Fmr1^{Flox/y}$ cKO mice.

MMP-9 can also regulate mTOR and Akt activation (Sidhu et al. 2014), potentially through integrins or BDNF/TrkB signaling (Hwang et al. 2005; Yang et al. 2009). Enhanced PI3K-Akt-mTOR signaling is implicated in FXS and may contribute to hyperexcitability by regulating protein synthesis through elongation factor 1α (Hou and Klann 2004; Ronesi and Huber 2008; Sharma et al. 2010; Gross et al. 2011; Hoeffer et al. 2012). The role of MMP-9 in FXS symptoms is further supported by the fact that the genetic deletion of MMP-9 activity in the brain of *Fmr1* KO mice restored dendritic spine development and mGluR5-dependent LTD in the hippocampus (Sidhu et al. 2014). In addition, MMP-9 reduction in the auditory cortex of *Fmr1* KO mice normalized auditory responses and the formation of WFA+ PNNs around PV

cells in the *Fmr1* KO mice to WT levels (Wen et al. 2018). MMP-9 deletion or reduction in the *Fmr1* KO mice also reversed ERP N1 amplitude habituation deficits (Lovelace et al. 2016) and reduced hyperexcitability in the developing auditory cortex (Wen et al. 2018), respectively. Minocycline, which is known to inhibit MMP-9 activity beside its antibiotic effects, was shown to reduce FXS symptoms in both humans (Schneider et al. 2013) and mice (Rotschafer et al. 2012; Dansie et al. 2013), further supporting the therapeutically targeting MMP-9 to alleviate FXS symptoms. While the present study suggests that loss of FMRP expression in excitatory neurons is sufficient to enhance gelatinase activity and affect formation of WFA+ PNNs around PV cells, the effects may be indirect and excitatory neurons may also modulate release of MMP-9 or MMP-2 from astrocytes. Future studies will test the role of astrocytes in regulating MMP-9 activity, PNNs and functional responses in the auditory cortex of the *Fmr1* KO mice.

Increased anxiety and locomotor activity are among the most consistent behavioral symptoms in individuals with FXS (Tranfaglia 2011). However, our studies show that forebrain excitatory neuron-specific $Cre^{Nex1}/Fmr1^{Flox/y}$ cKO mice only exhibit increased locomotor activity, but no anxiety-like behaviors. The auditory brainstem expresses high FMRP levels (Wang et al. 2014), and abnormal sensory processing at the level of the auditory brainstem may underlie the enhanced susceptibility to audiogenic seizures (Chen and Toth 2001). FMRP may regulate neuronal excitability through the direct interactions with several ion channels, such as sodium-activated potassium channel Slack, presynaptic N-type voltage-gated calcium channels, and calcium-activated potassium BK channels (Brown et al. 2010; Zhang et al. 2012; Deng et al. 2013; Ferron et al. 2014; Hébert et al. 2014; Myrick et al. 2015). The enhanced excitability is associated with behavioral symptoms observed in FXS, such as hyperactivity, anxiety, and seizures (Penagarikano et al. 2007; Braat and Kooy 2015). Brainstem noradrenergic and

serotoninergic systems may also contribute to anxiety phenotypes in FXS, which may be unaffected in the forebrain specific deletion model. Taken together, our results suggest the role of subcortical areas in regulating anxiety-like behaviors in global *Fmr1* KO mice as forebrain excitatory neuron specific deletion of FMRP is not sufficient to trigger this abnormal behavior. On the other hand, abnormal locomotor activity may depend on cortex-specific functions of FMRP.

FMRP loss from excitatory neurons in hippocampus and frontal cortex may also contribute to abnormal behaviors observed in *Fmr1* KO mice, such as hyperactivity, obsessive-compulsive behaviors, and learning and memory deficits (Dansie et al. 2013, Santos et al. 2014, Yau et al. 2018) Indeed FMRP loss is known to affect dendritic spine development in the excitatory neurons in the hippocampus (Sidhu et al. 2014) and mGluR5-dependent LTD in the CA1 hippocampal neurons (Huber et al. 2002). Future studies of changes in electrocortical activity in different areas of the brain using multi-electrode array EEGs and the analysis of mouse behaviors following cell- or brain area-specific deletion of FMRP would help us better understand the circuit level mechanisms.

Conclusions

Sensory processing issues are frequently associated with autism, but very little is known about underlying mechanisms. Humans with FXS show consistent and debilitating auditory hypersensitivity. Here we found that PV+ inhibitory neurons and the extracellular matrix structures that cover these cells are affected by *Fmr1* gene deletion in forebrain excitatory neurons, which is likely linked to reduced inhibition, abnormal resting low-gamma EEG power and hyperactive behaviors. Increased activity of extracellular matrix modifying enzyme (MMP-

9) may contribute to these deficits by cleaving aggrecan-containing WFA+ PNNs or signaling through cell surface receptors to mTOR/Akt pathway. Gamma synchronization, high-gamma power and anxiety-like behaviors were unaffected in $Cre^{Nex1}/Fmr1^{Flox/y}$ cKO mice. Together, these findings show that local cortical deficits contribute to many, but not all, phenotypes in the *Fmr1* KO mice and suggest cell-type and circuit specific contributions of the genetic mutation to various symptoms in FXS. The utility of identifying the relationships between cell type/circuit specificity and phenotypes in neurodevelopmental disorders is that therapeutic approaches can be potentially targeted to impact specific cell types, circuits and symptoms.

Acknowledgements

This work was supported by the National Institute of Child Health and Human Development and the National Institute of Mental Health (1U54 HD082008-01 to I.M.E., D.K.B., and K.A.R.); U.S. Army Medical Research and Materiel Command (W81XWH-15-1-0436 and W81XWH-15-1-0434 to I.M.E., D.K.B., and K.A.R.). The authors thank Klaus Nave (Göttingen, Germany) and Joshua Sanes (Harvard University) for providing breeding pairs of *Nex1(NeuroD6)*-Cre mice. We thank Dr. Christina Gross for her advice on FMRP staining. We also thank Camila Garcia Paz for technical support and members of the Ethell, Binder and Razak laboratories for helpful discussions and David Carter for advice on confocal microscopy.

Conflict of Interest

The authors declare no competing financial interests.

References

Anderson LA, Christianson GB, Linden JF. 2009. Mouse auditory cortex differs from visual and somatosensory cortices in the laminar distribution of cytochrome oxidase and acetylcholinesterase. *Brain Res*. 1252:130-142.

Antoine MW, Langberg T, Schnepel P, Feldman DE. 2019. Increased Excitation-Inhibition Ratio Stabilizes Synapse and Circuit Excitability in Four Autism Mouse Models. *Neuron*.

Artieda J, Valencia M, Alegre M, Olaziregi O, Urrestarazu E, Iriarte J. 2004. Potentials evoked by chirp-modulated tones: a new technique to evaluate oscillatory activity in the auditory pathway. *Clin Neurophysiol*. 115:699-709.

Atencio CA, Schreiner CE. 2008. Spectrotemporal processing differences between auditory cortical fast-spiking and regular-spiking neurons. *J Neurosci*. 28:3897-3910.

Balakrishnan S, Pearce RA. 2014. Spatiotemporal characteristics and pharmacological modulation of multiple gamma oscillations in the CA1 region of the hippocampus. *Front Neural Circuits*. 8:150.

Ballester-Rosado CJ, Albright MJ, Wu CS, Liao CC, Zhu J, Xu J, Lee LJ, Lu HC. 2010. mGluR5 in cortical excitatory neurons exerts both cell-autonomous and -nonautonomous influences on cortical somatosensory circuit formation. *J Neurosci*. 30:16896-16909.

Balmer TS. 2016. Perineuronal Nets Enhance the Excitability of Fast-Spiking Neurons. *eNeuro*. 3.

Beebe K, Wang Y, Kulesza R. 2014. Distribution of fragile X mental retardation protein in the human auditory brainstem. *Neuroscience*. 273:79-91.

1093 Bilousova TV, Dansie L, Ngo M, Aye J, Charles JR, Ethell DW, Ethell IM. 2009. Minocycline
1094 promotes dendritic spine maturation and improves behavioural performance in the fragile X
1095 mouse model. *J Med Genet*. 46:94-102.
1096 Braat S, Kooy RF. 2015. The GABAA Receptor as a Therapeutic Target for
1097 Neurodevelopmental Disorders. *Neuron*. 86:1119-1130.
1098 Brown MR, Kronengold J, Gazula VR, Chen Y, Strumbos JG, Sigworth FJ, Navaratnam D,
1099 Kaczmarek LK. 2010. Fragile X mental retardation protein controls gating of the sodium-
1100 activated potassium channel Slack. *Nat Neurosci*. 13:819-821.
1101 Brown RE, Corey SC, Moore AK. 1999. Differences in measures of exploration and fear in
1102 MHC-congenic C57BL/6J and B6-H-2K mice. *Behavior genetics*. 29:263-271.
1103 Cabungcal JH, Steullet P, Morishita H, Kraftsik R, Cuenod M, Hensch TK, Do KQ. 2013.
1104 Perineuronal nets protect fast-spiking interneurons against oxidative stress. *Proc Natl Acad Sci.*
1105 110:9130-9135.
1106 Cardin JA, Carlén M, Meletis K, Knoblich U, Zhang F, Deisseroth K, Tsai LH, Moore CI. 2009.
1107 Driving fast-spiking cells induces gamma rhythm and controls sensory responses. *Nature*.
1108 459:663-667.
1109 Carlén M, Meletis K, Siegle JH, Cardin JA, Futai K, Vierling-Claassen D, Rühlmann C, Jones
1110 SR, Deisseroth K, Sheng M, Moore CI, Tsai LH. 2012. A critical role for NMDA receptors in
1111 parvalbumin interneurons for gamma rhythm induction and behavior. *Mol Psychiatry*. 17:537-
1112 548.
1113 Castrén M, Pääkkönen A, Tarkka IM, Ryynänen M, Partanen J. 2003. Augmentation of auditory
1114 N1 in children with fragile X syndrome. *Brain Topogr*. 15:165-171.

1115 Chang MC, Park JM, Pelkey KA, Grabenstatter HL, Xu D, Linden DJ, Sutula TP, McBain CJ,
1116 Worley PF. 2010. Narp regulates homeostatic scaling of excitatory synapses on parvalbumin-
1117 expressing interneurons. *Nat Neurosci*. 13:1090-1097.
1118 Chen L, Toth M. 2001. Fragile X mice develop sensory hyperreactivity to auditory stimuli.
1119 *Neuroscience*. 103:1043-1050.
1120 Chen LY, Rex CS, Babayan AH, Kramár EA, Lynch G, Gall CM, Lauterborn JC. 2010.
1121 Physiological activation of synaptic Rac>PAK (p-21 activated kinase) signaling is defective in a
1122 mouse model of fragile X syndrome. *J Neurosci*. 30:10977-10984.
1123 Christie SB, Akins MR, Schwob JE, Fallon JR. 2009. The FXG: a presynaptic fragile X granule
1124 expressed in a subset of developing brain circuits. *J Neurosci*. 29:1514-1524.
1125 Contractor A, Klyachko VA, Portera-Cailliau C. 2015. Altered Neuronal and Circuit Excitability
1126 in Fragile X Syndrome. *Neuron*. 87:699-715.
1127 Crawford DC, Acuña JM, Sherman SL. 2001. FMR1 and the fragile X syndrome: human
1128 genome epidemiology review. *Genet Med*. 3:359-371.
1129 d'Ortho MP, Will H, Atkinson S, Butler G, Messent A, Gavrilovic J, Smith B, Timpl R, Zardi L,
1130 Murphy G. 1997. Membrane-type matrix metalloproteinases 1 and 2 exhibit broad-spectrum
1131 proteolytic capacities comparable to many matrix metalloproteinases. *Eur J Biochem*. 250:751-
1132 757.
1133 Dansie LE, Phommahaxay K, Okusanya AG, Uwadia J, Huang M, Rotschafer SE, Razak KA,
1134 Ethell DW, Ethell IM. 2013. Long-lasting effects of minocycline on behavior in young but not
1135 adult Fragile X mice. *Neuroscience*. 246:186-198.
1136 Del Pino I, García-Frigola C, Dehorter N, Brotons-Mas JR, Alvarez-Salvado E, Martínez de
1137 Lagrán M, Ciceri G, Gabaldón MV, Moratal D, Dierssen M, Canals S, Marín O, Rico B. 2013.

1138 Erbb4 deletion from fast-spiking interneurons causes schizophrenia-like phenotypes. *Neuron*.
1139 79:1152-1168.
1140 Deng PY, Rotman Z, Blundon JA, Cho Y, Cui J, Cavalli V, Zakharenko SS, Klyachko VA.
1141 2013. FMRP regulates neurotransmitter release and synaptic information transmission by
1142 modulating action potential duration via BK channels. *Neuron*. 77:696-711.
1143 Dvorak D, Fenton AA. 2014. Toward a proper estimation of phase-amplitude coupling in neural
1144 oscillations. *J Neurosci Methods*. 225:42-56.
1145 Dziembowska M, Pretto DI, Janusz A, Kaczmarek L, Leigh MJ, Gabriel N, Durbin-Johnson B,
1146 Hagerman RJ, Tassone F. 2013. High MMP-9 activity levels in fragile X syndrome are lowered
1147 by minocycline. *Am J Med Genet A*. 161A:1897-1903.
1148 Dziembowska M, Wlodarczyk J. 2012. MMP9: a novel function in synaptic plasticity. *Int J*
1149 *Biochem Cell Biol*. 44:709-713.
1150 Enriquez-Barreto L, Morales M. 2016. The PI3K signaling pathway as a pharmacological target
1151 in Autism related disorders and Schizophrenia. *Mol Cell Ther*. 4:2.
1152 Ethridge LE, White SP, Mosconi MW, Wang J, Byerly MJ, Sweeney JA. 2016. Reduced
1153 habituation of auditory evoked potentials indicate cortical hyper-excitability in Fragile X
1154 Syndrome. *Transl Psychiatry*. 6:e787.
1155 Ethridge LE, White SP, Mosconi MW, Wang J, Pedapati EV, Erickson CA, Byerly MJ, Sweeney
1156 JA. 2017. Neural synchronization deficits linked to cortical hyper-excitability and auditory
1157 hypersensitivity in fragile X syndrome. *Mol Autism*. 8:22.
1158 Ferron L, Nieto-Rostro M, Cassidy JS, Dolphin AC. 2014. Fragile X mental retardation protein
1159 controls synaptic vesicle exocytosis by modulating N-type calcium channel density. *Nat*
1160 *Commun*. 5:3628.

1161 Filice F, Vörckel KJ, Sungur A, Wöhr M, Schwaller B. 2016. Reduction in parvalbumin
1162 expression not loss of the parvalbumin-expressing GABA interneuron subpopulation in genetic
1163 parvalbumin and shank mouse models of autism. *Mol Brain*. 9:10.
1164 Fu Y, Kaneko M, Tang Y, Alvarez-Buylla A, Stryker MP. 2015. A cortical disinhibitory circuit
1165 for enhancing adult plasticity. *Elife*. 4:e05558.
1166 Gabel LA, Won S, Kawai H, McKinney M, Tartakoff AM, Fallon JR. 2004. Visual experience
1167 regulates transient expression and dendritic localization of fragile X mental retardation protein. *J*
1168 *Neurosci*. 24:10579-10583.
1169 Garcia-Pino E, Gessele N, Koch U. 2017. Enhanced Excitatory Connectivity and Disturbed
1170 Sound Processing in the Auditory Brainstem of Fragile X Mice. *J Neurosci*. 37:7403-7419.
1171 Gibson JR, Bartley AF, Hays SA, Huber KM. 2008. Imbalance of neocortical excitation and
1172 inhibition and altered UP states reflect network hyperexcitability in the mouse model of fragile X
1173 syndrome. *J Neurophysiol*. 100:2615-2626.
1174 Gkogkas CG, Khoutorsky A, Cao R, Jafarnejad SM, Prager-Khoutorsky M, Giannakas N,
1175 Kaminari A, Fragkouli A, Nader K, Price TJ, Konicek BW, Graff JR, Tzinia AK, Lacaille JC,
1176 Sonenberg N. 2014. Pharmacogenetic inhibition of eIF4E-dependent Mmp9 mRNA translation
1177 reverses fragile X syndrome-like phenotypes. *Cell Rep*. 9:1742-1755.
1178 Goebbels S, Bormuth I, Bode U, Hermanson O, Schwab MH, Nave KA. 2006. Genetic targeting
1179 of principal neurons in neocortex and hippocampus of NEX-Cre mice. *Genesis*. 44:611-621.
1180 Goel A, Cantu DA, Guilfoyle J, Chaudhari GR, Newadkar A, Todisco B, de Alba D, Kourdougli
1181 N, Schmitt LM, Pedapati E, Erickson CA, Portera-Cailliau C. 2018. Impaired perceptual learning
1182 in a mouse model of Fragile X syndrome is mediated by parvalbumin neuron dysfunction and is
1183 reversible. *Nat Neurosci*. 21:1404-1411.

1184 Gonzalez-Burgos G, Lewis DA. 2008. GABA neurons and the mechanisms of network
1185 oscillations: implications for understanding cortical dysfunction in schizophrenia. *Schizophr*
1186 *Bull*. 34:944-961.
1187 Gross C, Yao X, Pong DL, Jeromin A, Bassell GJ. 2011. Fragile X mental retardation protein
1188 regulates protein expression and mRNA translation of the potassium channel Kv4.2. *J Neurosci*.
1189 31:5693-5698.
1190 Hays SA, Huber KM, Gibson JR. 2011. Altered neocortical rhythmic activity states in Fmr1 KO
1191 mice are due to enhanced mGluR5 signaling and involve changes in excitatory circuitry. *J*
1192 *Neurosci*. 31:14223-14234.
1193 Hoeffer CA, Sanchez E, Hagerman RJ, Mu Y, Nguyen DV, Wong H, Whelan AM, Zukin RS,
1194 Klann E, Tassone F. 2012. Altered mTOR signaling and enhanced CYFIP2 expression levels in
1195 subjects with fragile X syndrome. *Genes Brain Behav*. 11:332-341.
1196 Hou L, Klann E. 2004. Activation of the phosphoinositide 3-kinase-Akt-mammalian target of
1197 rapamycin signaling pathway is required for metabotropic glutamate receptor-dependent long-
1198 term depression. *J Neurosci*. 24:6352-6361.
1199 Huber KM, Gallagher SM, Warren ST, Bear MF. 2002. Altered synaptic plasticity in a mouse
1200 model of fragile X mental retardation. *Proc Natl Acad Sci*. 99:7746-7750.
1201 Hwang JJ, Park MH, Choi SY, Koh JY. 2005. Activation of the Trk signaling pathway by
1202 extracellular zinc. Role of metalloproteinases. *J Biol Chem*. 280:11995-12001.
1203 Hébert B, Pietropaolo S, Même S, Laudier B, Laugeray A, Doisne N, Quartier A, Lefeuvre S,
1204 Got L, Cahard D, Laumonnier F, Crusio WE, Pichon J, Menuet A, Perche O, Briault S. 2014.
1205 Rescue of fragile X syndrome phenotypes in Fmr1 KO mice by a BKCa channel opener
1206 molecule. *Orphanet J Rare Dis*. 9:124.

1207 Janusz A, Milek J, Perycz M, Pacini L, Bagni C, Kaczmarek L, Dziembowska M. 2013. The
1208 Fragile X mental retardation protein regulates matrix metalloproteinase 9 mRNA at synapses. *J*
1209 *Neurosci*. 33:18234-18241.
1210 Kazdoba TM, Sunnen CN, Crowell B, Lee GH, Anderson AE, D'Arcangelo G. 2012.
1211 Development and characterization of NEX- Pten, a novel forebrain excitatory neuron-specific
1212 knockout mouse. *Dev Neurosci*. 34:198-209.
1213 Keeley S, Fenton AA, Rinzel J. 2017. Modeling fast and slow gamma oscillations with
1214 interneurons of different subtype. *J Neurophysiol*. 117:950-965.
1215 Kerrisk ME, Greer CA, Koleske AJ. 2013. Integrin α3 is required for late postnatal stability of
1216 dendrite arbors, dendritic spines and synapses, and mouse behavior. *J Neurosci*. 33:6742-6752.
1217 Kim H, Gibboni R, Kirkhart C, Bao S. 2013. Impaired critical period plasticity in primary
1218 auditory cortex of fragile X model mice. *J Neurosci*. 33:15686-15692.
1219 Klann E, Dever TE. 2004. Biochemical mechanisms for translational regulation in synaptic
1220 plasticity. *Nat Rev Neurosci*. 5:931-942.
1221 Legate KR, Wickström SA, Fässler R. 2009. Genetic and cell biological analysis of integrin
1222 outside-in signaling. *Genes Dev*. 23:397-418.
1223 Lensjø KK, Lepperød ME, Dick G, Hafting T, Fyhn M. 2017. Removal of Perineuronal Nets
1224 Unlocks Juvenile Plasticity Through Network Mechanisms of Decreased Inhibition and
1225 Increased Gamma Activity. *J Neurosci*. 37:1269-1283.
1226 Lovelace JW, Ethell IM, Binder DK, Razak KA. 2018. Translation-relevant EEG phenotypes in
1227 a mouse model of Fragile X Syndrome. *Neurobiol Dis*.

1228 Lovelace JW, Wen TH, Reinhard S, Hsu MS, Sidhu H, Ethell IM, Binder DK, Razak KA. 2016.
1229 Matrix metalloproteinase-9 deletion rescues auditory evoked potential habituation deficit in a
1230 mouse model of Fragile X Syndrome. *Neurobiol Dis*. 89:126-135.
1231 Lucas EK, Markwardt SJ, Gupta S, Meador-Woodruff JH, Lin JD, Overstreet-Wadiche L,
1232 Cowell RM. 2010. Parvalbumin deficiency and GABAergic dysfunction in mice lacking PGC-
1233 1α. *J Neurosci*. 30:7227-7235.
1234 Maris E, Oostenveld R. 2007. Nonparametric statistical testing of EEG- and MEG-data. *J*
1235 *Neurosci Methods*. 164:177-190.
1236 Martin del Campo HN, Measor KR, Razak KA. 2012. Parvalbumin immunoreactivity in the
1237 auditory cortex of a mouse model of presbycusis. *Hear Res*. 294:31-39.
1238 McRae PA, Baranov E, Sarode S, Brooks-Kayal AR, Porter BE. 2010. Aggrecan expression, a
1239 component of the inhibitory interneuron perineuronal net, is altered following an early-life
1240 seizure. *Neurobiol Dis*. 39:439-448.
1241 McRae PA, Rocco MM, Kelly G, Brumberg JC, Matthews RT. 2007. Sensory deprivation alters
1242 aggrecan and perineuronal net expression in the mouse barrel cortex. *J Neurosci*. 27:5405-5413.
1243 Mientjes EJ, Nieuwenhuizen I, Kirkpatrick L, Zu T, Hoogeveen-Westerveld M, Severijnen L,
1244 Rifé M, Willemsen R, Nelson DL, Oostra BA. 2006. The generation of a conditional Fmr1 knock
1245 out mouse model to study Fmrp function in vivo. *Neurobiol Dis*. 21:549-555.
1246 Miyata S, Kitagawa H. 2016. Chondroitin 6-Sulfation Regulates Perineuronal Net Formation by
1247 Controlling the Stability of Aggrecan. *Neural Plast*. 2016:1305801.
1248 Morawski M, Brückner G, Arendt T, Matthews RT. 2012. Aggrecan: Beyond cartilage and into
1249 the brain. *Int J Biochem Cell Biol*. 44:690-693.

1250 Murase S, Lantz CL, Kim E, Gupta N, Higgins R, Stopfer M, Hoffman DA, Quinlan EM. 2016.
1251 Matrix Metalloproteinase-9 Regulates Neuronal Circuit Development and Excitability. *Mol*
1252 *Neurobiol*. 53:3477-3493.
1253 Myrick LK, Deng PY, Hashimoto H, Oh YM, Cho Y, Poidevin MJ, Suhl JA, Visootsak J,
1254 Cavalli V, Jin P, Cheng X, Warren ST, Klyachko VA. 2015. Independent role for presynaptic
1255 FMRP revealed by an FMR1 missense mutation associated with intellectual disability and
1256 seizures. *Proc Natl Acad Sci*. 112:949-956.
1257 Niell CM, Stryker MP. 2010. Modulation of visual responses by behavioral state in mouse visual
1258 cortex. *Neuron*. 65:472-479.
1259 Nielsen DM, Derber WJ, McClellan DA, Crnic LS. 2002. Alterations in the auditory startle
1260 response in Fmr1 targeted mutant mouse models of fragile X syndrome. *Brain Res*. 927:8-17.
1261 Ozeki H, Finn IM, Schaffer ES, Miller KD, Ferster D. 2009. Inhibitory stabilization of the
1262 cortical network underlies visual surround suppression. *Neuron*. 62:578-592.
1263 Packer AM, Yuste R. 2011. Dense, unspecific connectivity of neocortical parvalbumin-positive
1264 interneurons: a canonical microcircuit for inhibition?. *J Neurosci*. 31:13260-13271.
1265 Patz S, Grabert J, Gorba T, Wirth MJ, Wahle P. 2004. Parvalbumin expression in visual cortical
1266 interneurons depends on neuronal activity and TrkB ligands during an Early period of postnatal
1267 development. *Cereb Cortex*. 14:342-351.
1268 Paxinos G, Franklin KB. 2004. The mouse brain in stereotaxic coordinates: Gulf professional
1269 publishing.
1270 Penagarikano O, Mulle JG, Warren ST. 2007. The pathophysiology of fragile x syndrome. *Annu*
1271 *Rev Genomics Hum Genet*. 8:109-129.

1272 Pizzorusso T, Medini P, Berardi N, Chierzi S, Fawcett JW, Maffei L. 2002. Reactivation of
1273 ocular dominance plasticity in the adult visual cortex. *Science*. 298:1248-1251.
1274 Purcell DW, John SM, Schneider BA, Picton TW. 2004. Human temporal auditory acuity as
1275 assessed by envelope following responses. *J Acoust Soc Am*. 116:3581-3593.
1276 Pérez-Alcázar M, Nicolás MJ, Valencia M, Alegre M, Iriarte J, Artieda J. 2008. Chirp-evoked
1277 potentials in the awake and anesthetized rat. A procedure to assess changes in cortical oscillatory
1278 activity. *Exp Neurol*. 210:144-153.
1279 Radwan B, Dvorak D, Fenton AA. 2016. Impaired cognitive discrimination and discoordination
1280 of coupled theta–gamma oscillations in Fmr1 knockout mice. *Neurobiol Dis*. 88:125-138.
1281 Rais M, Binder DK, Razak KA, Ethell IM. 2018. Sensory Processing Phenotypes in Fragile X
1282 Syndrome. *ASN Neuro*. 10:1759091418801092.
1283 Ray S, Maunsell JH. 2011. Different origins of gamma rhythm and high-gamma activity in
1284 macaque visual cortex. *PLoS Biol*. 9:e1000610.
1285 Rojas DC, Benkers TL, Rogers SJ, Teale PD, Reite ML, Hagerman RJ. 2001. Auditory evoked
1286 magnetic fields in adults with fragile X syndrome. *Neuroreport*. 12:2573-2576.
1287 Ronesi JA, Huber KM. 2008. Homer interactions are necessary for metabotropic glutamate
1288 receptor-induced long-term depression and translational activation. *J Neurosci*. 28:543-547.
1289 Rotschafer S, Razak K. 2013. Altered auditory processing in a mouse model of fragile X
1290 syndrome. *Brain Res*. 1506:12-24.
1291 Rotschafer SE, Marshak S, Cramer KS. 2015. Deletion of Fmr1 alters function and synaptic
1292 inputs in the auditory brainstem. *PLoS One*. 10:e0117266.
1293 Rotschafer SE, Razak KA. 2014. Auditory processing in fragile x syndrome. *Front Cell*
1294 *Neurosci*. 8:19.

1295 Rotschafer SE, Trujillo MS, Dansie LE, Ethell IM, Razak KA. 2012. Minocycline treatment
1296 reverses ultrasonic vocalization production deficit in a mouse model of Fragile X Syndrome.
1297 *Brain Res*. 1439:7-14.
1298 Roughley PJ, Mort JS. 2014. The role of aggrecan in normal and osteoarthritic cartilage. *J Exp*
1299 *Orthop*. 1:8.
1300 Santos AR, Kanellopoulos AK, Bagni C. 2014. Learning and behavioral deficits associated with
1301 the absence of the fragile X mental retardation protein: what a fly and mouse model can teach us.
1302 *Learn Mem*. 21:543-555.
1303 Sato A. 2016. mTOR, a Potential Target to Treat Autism Spectrum Disorder. *CNS Neurol Disord*
1304 *Drug Targets*. 15:533-543.
1305 Schneider A, Leigh MJ, Adams P, Nanakul R, Chechi T, Olichney J, Hagerman R, Hessl D.
1306 2013. Electrocortical changes associated with minocycline treatment in fragile X syndrome. *J*
1307 *Psychopharmacol*. 27:956-963.
1308 Selby L, Zhang C, Sun QQ. 2007. Major defects in neocortical GABAergic inhibitory circuits in
1309 mice lacking the fragile X mental retardation protein. *Neurosci Lett*. 412:227-232.
1310 Sharma A, Hoeffer CA, Takayasu Y, Miyawaki T, McBride SM, Klann E, Zukin RS. 2010.
1311 Dysregulation of mTOR signaling in fragile X syndrome. *J Neurosci*. 30:694-702.
1312 Sidhu H, Dansie LE, Hickmott PW, Ethell DW, Ethell IM. 2014. Genetic removal of matrix
1313 metalloproteinase 9 rescues the symptoms of fragile X syndrome in a mouse model. *J Neurosci*.
1314 34:9867-9879.
1315 Sinclair D, Oranje B, Razak KA, Siegel SJ, Schmid S. 2017. Sensory processing in autism
1316 spectrum disorders and Fragile X syndrome-From the clinic to animal models. *Neurosci*
1317 *Biobehav Rev*. 76:235-253.

1318 Sohal VS, Zhang F, Yizhar O, Deisseroth K. 2009. Parvalbumin neurons and gamma rhythms
1319 enhance cortical circuit performance. *Nature*. 459:698-702.
1320 Strumbos JG, Brown MR, Kronengold J, Polley DB, Kaczmarek LK. 2010. Fragile X mental
1321 retardation protein is required for rapid experience-dependent regulation of the potassium
1322 channel Kv3.1b. *J Neurosci*. 30:10263-10271.
1323 Sutcliffe JS, Nelson DL, Zhang F, Pieretti M, Caskey CT, Saxe D, Warren ST. 1992. DNA
1324 methylation represses FMR-1 transcription in fragile X syndrome. *Hum Mol Genet*. 1:397-400.
1325 Szklarczyk A, Lapinska J, Rylski M, McKay RD, Kaczmarek L. 2002. Matrix metalloproteinase-
1326 9 undergoes expression and activation during dendritic remodeling in adult hippocampus. *J*
1327 *Neurosci*. 22:920-930.
1328 Tallon-Baudry C, Bertrand O, Delpuech C, Pernier J. 1996. Stimulus specificity of phase-locked
1329 and non-phase-locked 40 Hz visual responses in human. *J Neurosci*. 16:4240-4249.
1330 Tamamaki N, Yanagawa Y, Tomioka R, Miyazaki J, Obata K, Kaneko T. 2003. Green
1331 fluorescent protein expression and colocalization with calretinin, parvalbumin, and somatostatin
1332 in the GAD67-GFP knock-in mouse. *J Comp Neurol*. 467:60-79.
1333 Tranfaglia MR. 2011. The psychiatric presentation of fragile x: evolution of the diagnosis and
1334 treatment of the psychiatric comorbidities of fragile X syndrome. *Dev Neurosci*. 33:337-348.
1335 Tsodyks MV, Skaggs WE, Sejnowski TJ, McNaughton BL. 1997. Paradoxical effects of external
1336 modulation of inhibitory interneurons. *J Neurosci*. 17:4382-4388.
1337 Veit J, Hakim R, Jadi MP, Sejnowski TJ, Adesnik H. 2017. Cortical gamma band
1338 synchronization through somatostatin interneurons. *Nat Neurosci*. 20:951-959.

1339 Verkerk AJ, Pieretti M, Sutcliffe JS, Fu YH, Kuhl DP, Pizzuti A, Reiner O, Richards S, Victoria
1340 MF, Zhang FP. 1991. Identification of a gene (FMR-1) containing a CGG repeat coincident with
1341 a breakpoint cluster region exhibiting length variation in fragile X syndrome. *Cell*. 65:905-914.
1342 Volman V, Behrens MM, Sejnowski TJ. 2011. Downregulation of parvalbumin at cortical
1343 GABA synapses reduces network gamma oscillatory activity. *J Neurosci*. 31:18137-18148.
1344 Wang J, Ethridge LE, Mosconi MW, White SP, Binder DK, Pedapati EV, Erickson CA, Byerly
1345 MJ, Sweeney JA. 2017. A resting EEG study of neocortical hyperexcitability and altered
1346 functional connectivity in fragile X syndrome. *J Neurodev Disord*. 9:11.
1347 Wang Y, Sakano H, Beebe K, Brown MR, de Laat R, Bothwell M, Kulesza RJ, Rubel EW. 2014.
1348 Intense and specialized dendritic localization of the fragile X mental retardation protein in
1349 binaural brainstem neurons: a comparative study in the alligator, chicken, gerbil, and human. *J*
1350 *Comp Neurol*. 522:2107-2128.
1351 Wen TH, Afroz S, Reinhard SM, Palacios AR, Tapia K, Binder DK, Razak KA, Ethell IM. 2018.
1352 Genetic Reduction of Matrix Metalloproteinase-9 Promotes Formation of Perineuronal Nets
1353 Around Parvalbumin-Expressing Interneurons and Normalizes Auditory Cortex Responses in
1354 Developing Fmr1 Knock-Out Mice. *Cereb Cortex*. 28:3951-3964.
1355 Wen TH, Binder DK, Ethell IM, Razak KA. 2018. The Perineuronal 'Safety' Net? Perineuronal
1356 Net Abnormalities in Neurological Disorders. *Front Mol Neurosci*. 11:270.
1357 Yan QJ, Asafo-Adjei PK, Arnold HM, Brown RE, Bauchwitz RP. 2004. A phenotypic and
1358 molecular characterization of the fmr1-tm1Cgr fragile X mouse. *Genes Brain Behav*. 3:337-359.
1359 Yan QJ, Rammal M, Tranfaglia M, Bauchwitz RP. 2005. Suppression of two major Fragile X
1360 Syndrome mouse model phenotypes by the mGluR5 antagonist MPEP. *Neuropharmacology*.
1361 49:1053-1066.

Yau SY, Bettio L, Vetrici M, Truesdell A, Chiu C, Chiu J, Truesdell E, Christie BR. 2018. Chronic minocycline treatment improves hippocampal neuronal structure, NMDA receptor function, and memory processing in Fmr1 knockout mice. *Neurobiol Dis*. 113:11-22.

Yang F, Je HS, Ji Y, Nagappan G, Hempstead B, Lu B. 2009. Pro-BDNF-induced synaptic depression and retraction at developing neuromuscular synapses. *J Cell Biol*. 185:727-741.

Yong VW, Krekoski CA, Forsyth PA, Bell R, Edwards DR. 1998. Matrix metalloproteinases and diseases of the CNS. *Trends Neurosci*. 21:75-80.

Zhang Y, Brown MR, Hyland C, Chen Y, Kronengold J, Fleming MR, Kohn AB, Moroz LL, Kaczmarek LK. 2012. Regulation of neuronal excitability by interaction of fragile X mental retardation protein with slack potassium channels. *J Neurosci*. 32:15318-15327.

Zorio DA, Jackson CM, Liu Y, Rubel EW, Wang Y. 2017. Cellular distribution of the fragile X mental retardation protein in the mouse brain. *J Comp Neurol*. 525:818-849.